

Ubiquitous evaluation of layer potentials using Quadrature by Kernel-Independent Expansion

Abtin Rahimian¹  · Alex Barnett² · Denis Zorin³

Received: 6 December 2016 / Accepted: 27 October 2017
© Springer Science+Business Media B.V., part of Springer Nature 2017

Abstract We introduce a quadrature scheme—QBKIX—for the *ubiquitous* high-order accurate evaluation of singular layer potentials associated with general elliptic PDEs, i.e., a scheme that yields high accuracy at all distances to the domain boundary as well as on the boundary itself. Relying solely on point evaluations of the underlying kernel, our scheme is essentially PDE-independent; in particular, no analytic expansion nor addition theorem is required. Moreover, it applies to boundary integrals with singular, weakly singular, and hypersingular kernels. Our work builds upon quadrature by expansion, which approximates the potential by an analytic expansion in the neighborhood of each expansion center. In contrast, we use a sum of fundamental solutions lying on a ring enclosing the neighborhood, and solve a small dense linear system for their coefficients to match the potential on a smaller concentric ring. We test the new method with Laplace, Helmholtz, Yukawa, Stokes, and Navier (elastostatic) kernels in two dimensions (2D) using adaptive, panel-based boundary quadratures on smooth and corner domains. Advantages of the algorithm include its relative simplicity of implementation, immediate extension to new kernels, dimension-independence

Communicated by Ralf Hiptmair.

✉ Abtin Rahimian
arahimian@acm.org

Alex Barnett
ahb@math.dartmouth.edu

Denis Zorin
dzorin@cims.nyu.edu

¹ Department of Computer Science, University of Colorado, Boulder, CO 80302, USA

² Department of Mathematics, Dartmouth College, Hanover, NH 03755, USA

³ Courant Institute of Mathematical Sciences, New York University, New York, NY 10003, USA

(allowing simple generalization to 3D), and compatibility with fast algorithms such as the kernel-independent FMM.

Keywords Boundary integral equations · High order quadrature · Kernel-independent · Near-singular integrals · Elliptic Boundary value problem

Mathematics Subject Classification 65R20

1 Introduction

The boundary integral method is a powerful tool for solving linear partial differential equations (PDEs) of classical physics with piecewise constant material coefficients, with applications including electromagnetic scattering, molecular electrostatics, viscous fluid flow, and acoustics. It involves expressing the solution as a convolution integral with a kernel function derived from the fundamental solution of the PDE [40] and an unknown “density” function defined on the domain boundaries or material interfaces, using the physical boundary condition to formulate an integral equation for this density, and finally obtaining a linear algebraic system via Galerkin, Nyström, or other discretization. Compared to commonly used differential formulations, boundary integral methods have a number of advantages: decreasing the dimension of the problem that needs to be discretized, avoiding meshing the volume, and improving conditioning. For instance, the integral equation can often be chosen to be a Fredholm equation of the second kind, resulting in a well-conditioned linear system which can be solved by a Krylov subspace methods in a few iterations. All these considerations are particularly important for problems with complicated and moving geometries [17, 29, 43, 48].

The main difficulty in using boundary integral methods is the need to evaluate singular and nearly-singular integrals: (i) Evaluating system matrix entries requires evaluation of the potential on the surface, which involves a *singular* integral; (ii) Once the density is solved for, the desired solution must still be evaluated in the form of a potential. As an evaluation point approaches the boundary of the domain, the peak in the resulting integrand becomes taller and narrower, giving rise to what is referred to as a *near-singular* integral. The result is an arbitrarily high loss of accuracy, if the distance from points to the surface is not bounded from below, when a quadrature scheme designed for smooth integrands is used [4, Section 7.2.1] [5].

Figure 1 illustrates the near-singular evaluation of the solution u of the Dirichlet Laplace equation in a simple smooth domain, which is represented by the double-layer potential

$$u(\mathbf{x}) = \frac{1}{2\pi} \int_{\Gamma} \frac{\partial}{\partial \mathbf{n}_y} \log \frac{1}{\|\mathbf{x} - \mathbf{y}\|} \phi(\mathbf{y}) \, ds(\mathbf{y}) , \quad (1.1)$$

where ϕ is the density defined on the boundary Γ . Various smooth quadrature rules are used for this integral. The growth in error as \mathbf{x} approaches Γ is apparent in all four plots (showing panel-based and global quadratures with different numbers of nodes N). Although the width of the high-error layer near the boundary shrinks like $1/N$ [5], the error always reaches $\mathcal{O}(1)$ at the boundary. The goal of this paper is to present

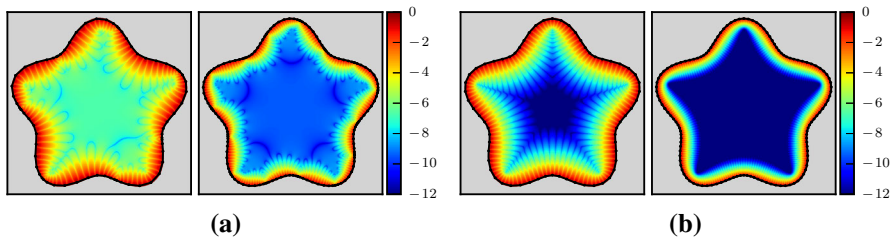


Fig. 1 Evaluation error plotted in the solution domain due to approximating the Laplace double-layer potential Eq. (1.1) using a quadrature designed for smooth functions. Logarithm of absolute error, $\log_{10} |\tilde{u}(\mathbf{x}) - u(\mathbf{x})|$, where u is the true solution and \tilde{u} is the discrete approximation using smooth quadrature is plotted for the case of constant density $\phi \equiv 1$. **a** Composite quadrature with $M = 7$ (left) or $M = 15$ (right) panels each with $q = 10$ Gauss–Legendre nodes. **b** Global composite trapezoid rule with $N = 64$ (left) or $N = 128$ (right) nodes

a flexible scheme that handles both tasks (singular and near-singular evaluation) to high-order accuracy in a kernel-independent (i.e., PDE-independent) manner.

Related work Designing quadrature schemes for singular and near-singular integrals has a long and rich history [4, 40]. Until recently, the quadrature methods were designed specifically for either on-surface evaluation or near-surface evaluation. Many of the on-surface integration quadrature are specific to a certain type of kernel (singularity), e.g., $\log |\mathbf{r}|$ in 2D or $1/|\mathbf{r}|$ in 3D [3, 12, 27, 33, 37, 39, 50, 51, 56]; the former case is reviewed in [26].

A popular method for on-surface quadrature is the product integration (in 2D, for the global trapezoid rule see [4, Section 4.2] or [40, Section 12.3], and for panel-based rules see [29]). In this context, an analytic convolution of the kernel with each function in some basis set is found, reducing evaluation of the integral to projection of the boundary density onto that basis set.

Another approach for on-surface evaluation is singularity subtraction, where the integrand is modified by subtracting an expression that eliminates its singularity [18, Chapter 2] and [31, 45]. However, this leaves high-order singularities in the kernel which makes the higher derivatives of the kernels unbounded, limiting the accuracy of the quadrature scheme. Alternatively, for weakly singular kernels, one can use transformations to cancel the singularity by the decay of area element (e.g., in 3D using Duffy transformation [19] or polar coordinates) [15, 21–24, 32, 35, 49, 55, 57]. To achieve a high convergence order, these methods need some form of partition of unity so that a high-order polar patch can be constructed around each point [57].

One can also regularize the kernel and then exploit quadrature schemes for smooth functions [41, 53]. However, to achieve higher accuracy, the effect of regularization needs to be corrected by using analytic expressions (e.g., asymptotic analysis) for the integrand [8]. Finally, there exist special high-order quadrature schemes for domains with corners, either via reparametrization [38, 40], panel-wise geometric refinement [28], or by custom generalized Gaussian quadratures [13, 14].

We now turn to near-singular integrals (evaluation close to the surface), which has traditionally been handled as a distinct task [7, 8, 25, 28, 29, 35, 52]. Beale and coauthors [9, 52, 58] use regularization methods to remove the singularity of the integral. To correct the error introduced by the regularization, they perform asymptotic analy-

sis and find correction expressions. Some authors used singularity cancellation (e.g., using local polar coordinates) in evaluating near-singular integrals [25, 35]. Interpolation along carefully-chosen lines connecting distant points (where a smooth quadrature is accurate) to an on-surface point has also been successful [46, 57].

Recently, unified approaches to on-surface and close evaluation have been proposed, the first being the 2D Laplace high-order global and panel-based quadratures of Helsing and Ojala [29]. This approach has been extended to near-singular Stokes single- and double-layer kernels with global [7] and panel-based [43] quadrature. The use of *local expansions*—analytic separation of variables to the PDE solutions analogous to a Taylor series in the complex plane—for the evaluation of integrals near the boundary was introduced in [5].

In the scheme proposed in [5], a refined smooth quadrature is needed to accurately evaluate the expansion coefficients via the addition theorem. It was observed that the expansion can also be used to evaluate at target points on the boundary of the domain, if certain conditions are satisfied [20]; this was used to construct a unified quadrature scheme—Quadrature by Expansion (QBX)—for near and on-surface evaluation of integrals [36]. Rachh et al. [47] recently showed how to efficiently combine QBX evaluations with the fast multipole method.

However, powerful as they are, QBX schemes require both a local expansion and addition theorem particular to each PDE, which would be algebraically tedious especially for vector-valued PDEs such as Stokes and elastostatics. This motivates the need for a scheme that can handle multiple PDEs without code changes. The present work fills this gap.

Overview and model problems As with QBX, we construct an approximate representation for PDE solutions in a small region abutting the boundary, then use it for near and on-surface evaluations. However, in contrast to QBX, our representation is an *equivalent density* on a closed curve enclosing this region; when discretized, this gives a ring of “proxy” point sources (also known as the *method of fundamental solutions* [10]). Matching is done at a second smaller ring of “check” points where a refined smooth quadrature is accurate, thus the only dependence on the PDE is via point-to-point kernel evaluations—the method is kernel-independent, and essentially PDE-independent.

We focus on Dirichlet boundary-value problems

$$\mathcal{L}u = 0 \quad \text{in } \Omega, \quad (1.2)$$

$$u = f \quad \text{on } \Gamma, \quad (1.3)$$

where Ω is a simply-connected interior domain with smooth boundary Γ , for the following partial differential operators:

$$\mathcal{L}u = \begin{cases} \Delta u & \text{Laplace,} \\ (\Delta - \lambda^2)u & \text{Yukawa,} \\ (\Delta + \omega^2)u & \text{Helmholtz } (\text{Im } \omega \geq 0), \\ \Delta u - \nabla p & \text{Stokes (subject to } \nabla \cdot u = 0), \\ \Delta u + \frac{1}{1-2\nu} \nabla \nabla \cdot u & \text{Elastostatic.} \end{cases} \quad (1.4)$$

To obtain well-conditioned formulations of the problem, we represent the solution of Eqs. (1.2–1.4) for $\mathbf{x} \in \Omega$ by the double-layer potentials

$$u(\mathbf{x}) = \mathcal{D}[\phi](\mathbf{x}) := \int_{\Gamma} \frac{\partial \Phi(\mathbf{x}, \mathbf{y})}{\partial \mathbf{n}_{\mathbf{y}}} \phi(\mathbf{y}) \, ds(\mathbf{y}), \quad (1.5)$$

where Φ is the fundamental solution for the operator \mathcal{L} , and ϕ is an unknown density. The fundamental solutions for the operators listed in Eq. (1.4) are given in “Appendix A”. A standard step (see, e.g., [30]) is now to substitute Eq. (1.5) into the boundary condition and use the jump relation for the potential to obtain the second-kind integral equation

$$-\frac{1}{2}\phi(\mathbf{x}) + (D\phi)(\mathbf{x}) = f(\mathbf{x}), \quad \text{for } \mathbf{x} \in \Gamma, \quad (1.6)$$

where D is the restriction of \mathcal{D} to the curve. Here, the integral implicit in the integral operator D must be taken in the principal value sense.

Discretization and overall approach In general, a smooth quadrature is a set of nodes $\mathbf{x}_i \in \Gamma$ with associated weights w_i , such that

$$\int_{\Gamma} f \, ds \approx \sum_{i=1}^N w_i f(\mathbf{x}_i), \quad (1.7)$$

holds to high accuracy for smooth functions on Γ —including the density ϕ . In this work, we use q -node Gauss–Legendre quadrature scheme on panels, and for convergence tests, we increase the number of panels while holding q fixed. Upon discretization, Eq. (1.6) will be approximated by the linear system

$$\sum_{j=1}^N A_{ij} \phi_j = f(\mathbf{x}_i), \quad i = 1, \dots, N, \quad (1.8)$$

whose solution $\boldsymbol{\phi} = \{\phi_j\}_{j=1}^N$ approximates the density values at the collocation points. In practice, for large problems, the matrix A is not constructed explicitly, but instead the matrix-vector product $A\boldsymbol{\phi}$ is evaluated using the fast multipole method. We test the QBKIX scheme both for applying matrix A (i.e., on-surface evaluation) and evaluating the solution at arbitrary points, near-evaluation in particular.

The system matrix elements are computed using the Nyström method [40, Ch. 12]. If the operator D is smooth on $\Gamma \times \Gamma$, we use a smooth Nyström formula; e.g., for Laplace,

$$A_{ij} = \begin{cases} \frac{\partial \Phi(\mathbf{x}_i, \mathbf{x}_j)}{\partial \mathbf{n}_{\mathbf{x}_j}} w_j, & i \neq j, \\ -\frac{1}{2} - \frac{\kappa(\mathbf{x}_j)}{4\pi} w_j, & i = j, \end{cases} \quad (1.9)$$

where $\kappa(\mathbf{x})$ is the curvature at $\mathbf{x} \in \Gamma$. For a Gauss–Legendre quadrature scheme, one may achieve high-order convergence in N ; if a spectral quadrature is used, super-

algebraic convergence is possible. However, for Yukawa and Helmholtz in 2D, and all 3D elliptic kernels, singular quadrature is needed for high-order accuracy.

In contrast to established approaches using specialized singular quadratures, we follow the idea underlying the QBX method: *applying A to a vector ϕ is equivalent to evaluating the interior limit of the double-layer potential due to a smooth density interpolated from ϕ* . This observation leads to the QBKIX idea: use a fast algorithm combined with the smooth quadrature scheme, Eq. (1.7), for point evaluation *away* from the surface—at points we refer to as *check points*—and interpolate from these points to the on surface point, to compute $A\phi$ for the Krylov iteration. As this interpolation can be done using points on one or both sides of the surface, in Sect. 4.2 we compare “one-sided” and “two-sided” variants of QBKIX with respect to their spectra and iterative convergence rates.

Although we are focusing on interior Dirichlet tests and Nyström-style sampled representation of the density in this work, QBKIX is applicable for Neumann or other boundary conditions, and Galerkin and other discretization types. Moreover, while the approach presented in this paper is restricted to 2D, there is no fundamental obstacle to an extension to 3D.

The rest of the paper is structured as follows. In Sect. 2 we present the QBKIX algorithm for integration. We present an error analysis in Sect. 3. In Sect. 4, and report the results of numerical experiments quantifying the accuracy of the method for a number of representative problems.

2 Algorithms

Given a closed curve $\Gamma \subset \mathbb{R}^2$ with interior Ω , and Dirichlet data f on Γ , our goal is to numerically solve the integral equation (1.6) for density and evaluate the solution of the underlying PDE at an arbitrary target point $\mathbf{x} \in \overline{\Omega}$. We assume that Γ is parametrized by a 2π -periodic piecewise-smooth function $X(t)$, so that the arc length element is $ds = |X'(t)| dt$, $|X'(t)|$ is bounded from below, and that $X(t)$ and the data function $f(t)$ may be evaluated at any $t \in [0, 2\pi)$. The boundary is subdivided into *panels*, which can be of different lengths, on which the smooth quadrature rule is defined (we use Gauss–Legendre quadrature), at q nodes \mathbf{x}_j per panel. We assume that the density is available as a vector of samples $\phi(\mathbf{x}_j)$ at the quadrature nodes.

2.1 Single-point evaluation

We describe our method in the simplest form for computing the solution accurately at a given point \mathbf{x} . We assume that there is a single point on Γ closest to \mathbf{x} , on a panel of length L . We assume that at a distance 2δ along the normal to the panel at any point, the smooth quadrature meets the target accuracy of evaluation, so the distance from \mathbf{x} to the surface is less than 2δ . We discuss how δ is chosen and how to ensure that this condition holds after the algorithm formulation.

The local geometric configuration of various types of points we are using in our algorithm is shown in Fig. 2. The setup shown in the image is for computing the

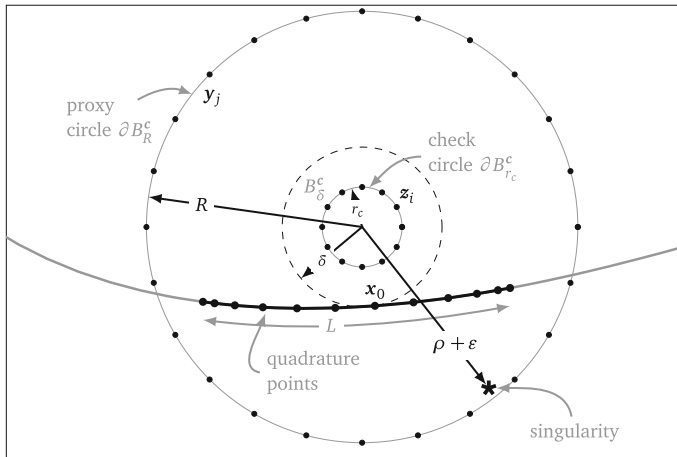


Fig. 2 Schematic of a kernel-independent expansion. Geometry of QBKIX, with proxy and check circles centered at c near a panel of length L of the boundary Γ discretized with q Gauss–Legendre sample points. The evaluation domain B_δ^c is a disc centered at c of radius δ (dashed circle abutting the boundary at x_0). The points z_i are the check points on the circle $\partial B_{r_c}^c$ of radius r_c , and y_j are the proxy points on the circle ∂B_R^c of radius R . For error analysis, the singularities of the exact solution are assumed to be at a distance farther than ρ from c . Note that, for clarity, the relative sizes of circles and distances between sample points are different from the ones actually used

potential accurately for any point x inside a disk B_δ^c of radius δ centered at c , touching the surface at a point x_0 on a panel of length L .

The points we use in the algorithm are placed on two concentric circles with the same center as the evaluation disk B_δ^c . The *proxy points* on a circle ∂B_R^c of a radius $R > \delta$, where we compute *equivalent density* values, are used to approximate the solution inside B_δ^c . The *check points* z_i are on a circle $\partial B_{r_c}^c$ of a radius $r_c < \delta$. At these points, we evaluate the solution accurately by using a smooth quadrature on a set of smaller panels obtained by splitting each original panel to β smaller panels. The check points are used to compute the equivalent density values at the proxy points as described below.

The algorithm depends on a number of parameters; these parameters need to be chosen appropriately to achieve an overall target accuracy. Specific choices are discussed in the next section. The key steps in the algorithm are

- (1) *Set-up of proxy and check points.* We choose a center $c \in \Omega$ at a distance δ from Γ , such that x is no further from c than δ . E.g., for $x \in \Gamma$, we set $c = x - \delta n$, where n is the outward normal. n_p proxy points y_j are arranged equally on the circle of radius R with center c , where $R > \delta$ is of order L . Similarly n_c check points z_i are arranged on the concentric circle of radius $r_c < \delta$ (Fig. 2).
- (2) *Upsampling the density.* Each panel is split into β panels corresponding to equal ranges of t , to give a set of βN fine-scale nodes \tilde{x}_l with weights \tilde{w}_l . The global factor β is chosen so that the solution can be evaluated accurately at the check points, i.e., at a distance $\delta - r_c$ from the surface. The density is interpolated from its original samples $\phi(x_j)$ on each panel, using q th order Lagrange interpolation

to the fine-scale nodes, to give the refined vector of samples $\tilde{\phi}_l, l = 1, \dots, \beta N$. Alternative to panel splitting, one can use a higher order panel with βN nodes at this step. We opted for the former due to its simpler implementation.

- (3) *Direct upsampled evaluation at check points.* The integral is evaluated at each check point z_i using the fine-scale boundary smooth quadrature:

$$\tilde{u}(z_i) = \sum_{l=1}^{\beta N} \frac{\partial \Phi(z_i, \mathbf{x}_l)}{\partial \mathbf{n}_{\mathbf{x}_l}} \tilde{\phi}_l \tilde{w}_l. \quad (2.1)$$

Denote by $\tilde{\mathbf{u}} := \{\tilde{u}(z_i)\}_{i=1}^{n_c}$ the column vector of these values at the check points.

- (4) *Solving for the equivalent density values.* Next, we construct an $n_c \times n_p$ matrix Q with elements

$$Q_{ij} = \Phi(z_i, \mathbf{y}_j). \quad (2.2)$$

Applying Q to a vector of density values at proxy points computes a periodic trapezoidal rule approximation to the single-layer potential corresponding to this density evaluated at check points. Then we solve a small, dense, and ill-conditioned linear system

$$Q\alpha = \tilde{\mathbf{u}}, \quad (2.3)$$

in the least-squares sense, to get the set of proxy density values $\alpha := \{\alpha_j\}_{j=1}^{n_p}$. The ill-conditioning arises from the exponential decay of singular values in the single-layer operator between concentric circles (see Fig. 4). Despite this, if Eq. (2.3) is solved in a backward-stable manner, a high-accuracy result is obtained (cf. [6], we explain the details below for completeness).

- 5 *Evaluation of the proxy sources at the target.* Finally, the equivalent density is evaluated at the target \mathbf{x} ,

$$\hat{u}(\mathbf{x}) = \sum_{j=1}^{n_p} \alpha_j \Phi(\mathbf{x}, \mathbf{y}_j), \quad (2.4)$$

We may view this as an approximation for the true solution u in the basis of fundamental solutions centered at the proxy points, that holds to high accuracy in the disk B_δ^c .

Figure 3 illustrates the stages of QBKIX evaluation for a set of target points lying in a single disk B_δ^c . The final evaluation of Eq. (2.4) over the disc of target points has around 12 digits of accuracy.

Handling the ill-conditioned linear solves The ill-conditioned system Eq. (2.3) is solved by applying a regularized pseudo-inverse, as follows. Let $\varepsilon_{\text{pinv}}$ be the desired relative accuracy for inversion; typically we set $\varepsilon_{\text{pinv}} = 10^{-14}$. Then, taking the singular value decomposition (SVD) [54] $Q = U\Sigma V^*$ with $\Sigma = \text{diag}\{\sigma_j\}$ being the diagonal matrix of singular values, we write $\Sigma^\dagger := \text{diag}\{\sigma_j^\dagger\}$ where

$$\sigma_j^\dagger = \begin{cases} \sigma_j^{-1}, & \sigma_j > \varepsilon_{\text{pinv}} \sigma_1, \\ 0, & \text{otherwise.} \end{cases} \quad (2.5)$$

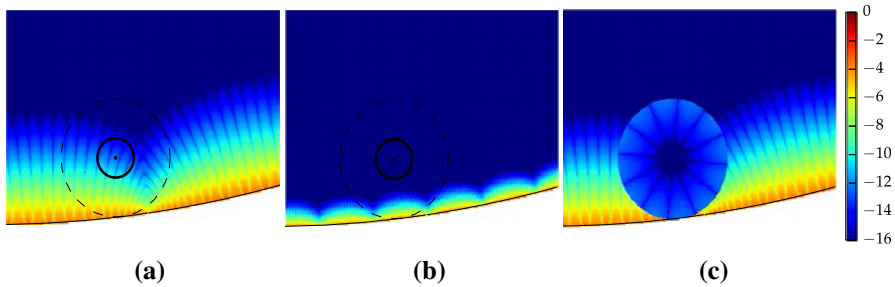


Fig. 3 Stages of QBKIX construction. The stages given in Sect. 2 are illustrated using plots of the \log_{10} of the evaluation error near a boundary (full boundary is shown in Fig. 9), for the double-layer density $\phi \equiv 1$ for Laplace's equation. The evaluation disc B_δ^c (dashed circle), check circle $\partial B_{r_c}^c$ (solid circle) are shown, and proxy points are not shown. The stages of the algorithm as well as the geometry of the QBKIX expansion are kernel-independent—the accuracy of the solution depends on the problem

Then we use the solution

$$\alpha := V(\Sigma^\dagger U^* \mathbf{u}). \quad (2.6)$$

Note that the matrices U^* and V must be applied in two separate steps (as indicated by the parenthesis) for backward stability [54], since a matrix-vector multiply with the single pseudo-inverse matrix $Q^\dagger := V \Sigma^\dagger U^*$ is unstable due to round-off error caused by its large entries. If k is the number of singular values greater than $\varepsilon_{\text{pinv}}$, i.e., the numerical $\varepsilon_{\text{pinv}}$ -rank of the matrix Q , the factors V and U^* have sizes $n_p \times k$ and $k \times n_c$ respectively.

Parameter summary The algorithm described above uses a number of parameters, which we summarize here.

The following parameters are defined globally:

- The quadrature order q , which determines the number of samples per panel, and both far-field evaluation accuracy and, together with β , the accuracy of evaluation at check points. This parameter is selected arbitrarily based on the desired overall accuracy. We use $q = 16$, which is sufficient for full double precision of integration in the far field.
- The numbers of proxy points n_p and check points n_c ; the former determines how accurate the approximation inside B_δ^c can be and the latter is chosen to have enough sampling.
- The panel refinement factor β which needs to be chosen to maintain desired accuracy for check point evaluation.

Three additional parameters, the accurate evaluation distance δ , the proxy point circle radius R and the check point circle radius r_c , are panel-dependent, and are chosen with respect to the length of the nearest panel L . A careful choice of all of these, as fractions of L , is needed to achieve a target error without requiring excessive refinement. We discuss the choice of these parameters in Sect. 3.

Defining panels In our experiments, we consider two ways of defining panels. The first approach is primarily needed to understand the convergence of the method with respect to the number of panels, i.e., for a given number of panels, we determine

the error. In this case, we simply partition the parametric domain of $X(t)$ into M equal-sized intervals, with one panel corresponding to each interval. We assume the parametrization to be sufficiently close to an arclength parametrization, so that the panel length has little variation, and choose M to be fine enough so that the geometric condition on the check points is satisfied.

In a more practical scenario, when a target error is specified, we need to determine panel sizes adaptively. The key requirement that needs to be satisfied by panels is that the accuracy of check-point evaluation at stage 2 matches the target accuracy in the far field (i.e., points farther than 2δ from the boundary). The adaptive refinement starts with one panel covering the entire boundary, then recursively splitting panels into two equal pieces in parameter t , until all panels are deemed *admissible* or their length is less than a set tolerance ε_l .

A panel is admissible if

- (i) the interpolation of $X(t)$ and $f(t)$ from a q -node panel at the collocation points of the two q -nodes Gauss–Legendre panels (obtained by splitting the coarse panel to two pieces) matches the direct evaluation of X and f on the finer nodes, to a maximum absolute tolerance ε_a , which we choose as 10^{-11} unless stated otherwise;
- (ii) it is no more than twice the arc length of that of its neighbors;
- (iii) the length of the panel does not exceed a given fraction of the minimal radius of curvature at a point of the panel, or is less than a minimal length ε_l set by the user (which can be chosen proportional to the desired error for a smooth quadrature); and
- (iv) any check point corresponding to a point \mathbf{x} is not closer than $\delta - r_c$ to any point on the surface.

The relationship between a panel and its children implies a binary tree over the boundary. The second criterion ensures that the panels are the leaves of a *balanced* binary tree, which is needed for accurate evaluation of integrals at the check points, by ensuring that, after upsampling by the factor β , check points from a panel are in the accurate region of the panel's immediate neighbors. For domains with sharp corners, the forth and second conditions imply dyadic refinement of panel length bounded below by panel minimum length ε_l .

To check criterion (iv), it is sufficient to check the distance of the center of expansion \mathbf{c} from the boundary and ensure that $|\mathbf{c} - \mathbf{x}| \geq |\mathbf{c} - \mathbf{x}'|$ for all $\mathbf{x}' \in \Gamma$. To this end, we use a uniform grid of size proportional the average value of δ to quickly find panels that may violate the condition (the exact value of grid spacing affects efficiency and not accuracy). We insert the bounding boxes of panels as well as the bounding boxes for discs B_δ^c into the grid. Then, we compute the distance of \mathbf{c} to panels whose bounding box intersects the grid boxes covering B_δ^c . If the distance is less than δ for a point other than \mathbf{x} , that panel is mark to be divided.

In both cases, the result is a set of N nodes $\mathbf{x}_j = X(t_j)$, where t_j are the parameter values of the nodes, with weights $w_j = |X'(t_j)|w'_j$ where w'_j are the Gauss–Legendre weights scaled by the panel parametric lengths. This smooth quadrature approximates the boundary condition f with target accuracy ε_a . When the domain is smooth, the density ϕ solving Eq. (1.6) is just as smooth as f : since D is compact, Eq. (1.6) satisfies

the Fredholm alternative, meaning that $(-1/2 + D) : H^s \rightarrow H^s$ is one-to-one and onto, for any Sobolev order s (see [40, p. 215]). Thus the approximation accuracy of ϕ is similar to that of f .

2.2 On-surface evaluation for iterative solution of the linear system

As discussed in the introduction, one context where singular quadratures are needed is for applying A , the matrix discretization of the operator $(-\frac{1}{2}I + D)$, to the current density vector ϕ during the iterative solution of Eq. (1.8). This matrix-vector multiplication is equivalent to evaluation of the interior limit of the double-layer potential at the nodes due to the smooth interpolant of the density vector. As with QBX [36, Sec. 3.5], one may exploit this in two different ways.

- One-sided QBKIX: as stated above, we use the interior limit of the potential at the nodes for $A\phi$.
- Two-sided QBKIX: we average the interior and exterior limits of the potential at the nodes, which, by canceling the jump relation terms, applies a matrix approximation to the operator D . We then explicitly add $-\frac{1}{2}\phi$ to the answer.

Although mathematically equivalent, these two variants smooth high-frequency components in the density differently: one-sided QBKIX tends to dampen these components, leading to an accumulation of eigenvalues of A around zero. This has a negative impact on convergence. In contrast, for two-sided QBKIX, since the approximation of D tends to damp high-frequency components, the explicit inclusion of $-\frac{1}{2}I$ ensures that these components end up being multiplied by a number very close to $-\frac{1}{2}$, which leads to better clustering of the spectrum and improved convergence rates. We present a numerical comparison of these two alternatives in Sect. 4.2.

2.3 Efficiency considerations and computational complexity

Given a set of evaluation points \mathbf{x} , the brute-force approach is to run the algorithm described above, including construction of check and proxy points, for each sample point separately. This is highly inefficient, and the following obvious optimizations can be applied:

- The upsampled density on the fine-scale nodes need be computed only once.
- The SVD of matrices Q may be precomputed. For translation- and scale-invariant kernels, (i.e., all kernels we consider except Yukawa and Helmholtz) these matrices do not depend on the choice of the center and circle radii, as long as the ratio R/r_c is fixed.
- One may use the kernel-independent FMM method for evaluation of the solution at the check points for all target points at once.

We consider the complexity of using QBKIX for the task of on-surface evaluation at all boundary nodes $\mathbf{x} \in \Gamma$. For a boundary with M panels and q -node Gauss–Legendre quadrature on each, there are $N = Mq$ nodes in total. We use a conservative assumption that a distinct set of check and proxy points is used for each of the targets. Then, using KIFMM, the evaluation of the boundary integral from the β -refined

boundary to the check points is $\mathcal{O}((\beta + n_c)N)$. We assume that the factorization of the pseudo-inverse for computing the equivalent densities α is precomputed. The cost of applying the factors V and U^* , of sizes $n_p \times k$ and $k \times n_c$, for targets point is $\mathcal{O}(k(n_c + n_p)N)$. The cost of evaluation of the approximation from proxy density values at target points is $\mathcal{O}(Nn_p)$.

We conclude that the overall cost is $\mathcal{O}((\beta + n_c + kn_c + kn_p + n_p)N)$, which for typical choices $\beta = 4$ and $n_c = 2n_p$ reduces to $\mathcal{O}(kn_pN)$. We see that the scheme is linear in N , but with a prefactor of order k^2 (since, as discussed in the next section, n_p is of order k). The two-sided variant involves another overall factor of 2.

If the same check and proxy points are used for a number of targets, an additional, potentially very large, constant-factor speedup can be obtained. The speedup factor is proportional to the average number of targets handled by each set of check and proxy points.

3 Error analysis and parameter choices

In this section, we present theoretical results, focusing on the cases of scalar u governed by the Laplace equation $\Delta u = 0$, or by the Helmholtz equation $(\Delta + \omega^2)u = 0$ for real ω . We expect similar results for the other elliptic PDEs in Eq. 1.4.

We split QBKIX into two stages: (i) evaluation of u on the check points using a refined smooth quadrature, with the associated error e_c ; (ii) solution of a small linear system to determine the equivalent density values α at the proxy points that best represent u at the check points. This is followed by evaluating the approximation of u at target points using these density values.

At the first stage, the error e_c is effectively the smooth quadrature error of the refined panels. The primary focus of our analysis is on the second stage. We analyze the error behavior in the idealized situation of exact arithmetic and infinitely many check points, obtaining the dependence of the second-stage error e on δ , R , ρ , and n_p . We then describe a heuristic model for the effects of finite-precision computations, which adds an extra term to e , depending on e_c , δ , r_c , and k .

We use the overall error model, along with experiments, to provide a choice of the various parameters in the scheme resulting in the on- and near-surface evaluation errors of the same magnitude as the far-field integration errors.

3.1 Error at check points

Recall that evaluation of u on the check points is done by approximating the exact integral Eq. (1.5) by Eq. (2.1) using q -node Gauss–Legendre quadrature on panels (subdivided by factor β). We state a theorem adapted from [36, Theorem 1] (specifically, taking the quadrature error term for $p = 0$), which uses classical quadrature error bounds. It was proven in the context of the Helmholtz equation.

Theorem 3.1 ([36]) *Let L be the arc-length of a panel Γ subdivided equally (with respect to parameterization) into $\beta \in \mathbb{N}$ segments, on each of which a q -node Gauss–Legendre quadrature rule is used. Let the density be $\phi \in C^{2q+1}(\Gamma)$. Then*

the quadrature error for Eq. (2.1) at a target point z_i a distance d from Γ obeys

$$e_c \leq C_{\Gamma,q} \left(\frac{L}{4\beta d} \right)^{2q} \|\phi^{(2q+1)}\|_{L_\infty(\Gamma)}, \quad (3.1)$$

where $C_{\Gamma,q}$ depends on the panel and the order q , but not on β or d .

Thus, at fixed q , panel size L , and target distance d , error vanishes with order $2q$ with respect to the upsampling β . It is conjectured that this holds for other standard PDE kernels. In our application, panels are adaptively refined, so that they are relatively flat (the radius of curvature exceeds δ), ensuring that $d = \delta - r_c$ is the closest distance of the check points to the panel. As discussed in Sect. 3.4, we will fix d/L , by choosing the evaluation disk radius δ and the checkpoint circle radius r_c as fractions of L . Thus, by choosing the refinement factor β high enough one can lower e_c to close to machine precision. For instance, when $q = 16$, it is sufficient to use $L/(4\beta d) = 1/2$, to obtain an error on the order of 10^{-10} at distance d from the panel.

Note that the above theorem is pessimistic, because of rapid growth of the derivatives due to the nearby singularity in the analytic continuation of the integrand [2, Sect. 3.1.1]. af Klinteburg and Tornberg have proven better error estimates for the Laplace and Helmholtz equations, both for flat panels [2], and for curved panels [1], that capture the exponential convergence with respect to q when all other parameters are fixed, and have sharp constants. These may be viewed as panel-wise versions of Laplace periodic trapezoid rule exponential convergence results of the second author [5, Theorems 2.3 and 2.9]. However, Theorem 3.1 will be sufficient for our purposes.

3.2 Error of the proxy point representation in exact arithmetic

Next, we analyze the dependence of the error (computed in exact arithmetic) of the second stage of QBKIX on the number of proxy points n_p , the proxy circle radius R , and the distance $r \leq \delta$ from the center c to the evaluation point.

Let \hat{u} be given by the proxy representation, Eq. (2.4), with equivalent density values α_j at proxy points y_j , $j = 1, \dots, n_p$. We consider evaluation of the approximation \hat{u} in B_r^c , the disc of radius r centered at c , given correct values for u at a very large number of check points n_c , so that we can replace the discrete least-squares problem we solve with a continuous one.

Let the equivalent densities α_j be chosen to minimize the L^2 error on the check circle, i.e.,

$$\alpha = \arg \min_{\alpha \in \mathbb{C}^{n_p}} \|\hat{u} - u\|_{L_2(\partial B_r^c)}. \quad (3.2)$$

By convergence of the periodic trapezoidal quadrature on the check points, this corresponds to the $n_c \rightarrow \infty$ limit of the QBKIX scheme. Let

$$e(r) := \sup_{x \in \partial B_r^c} |\hat{u}(x) - u(x)|, \quad (3.3)$$

be the upper bound on the pointwise error in the part of the disc lying inside the closure of the domain. Below we give bounds on e when u is sufficiently regular, meaning that any singularities in the continuation of u exceed some distance $\rho > \delta$ from the center of the expansion \mathbf{c} .

As a toy model, it is instructive to consider the case of \hat{u} generated by a continuous single-layer potential on the circle of radius R , with density $\psi(\theta) = \sum_{n \in [-n_p/2, n_p/2]} \psi_n e^{in\theta}$, i.e. Fourier modes up to the Nyquist frequency $n_p/2$. The estimates we derive in this case will be used in the proof of the general theorem.

Following [6] (including a prefactor $1/R$ in the layer potential), the linear map from $\psi(\theta)$ to the solution values at radius r_c is diagonal in the Fourier basis, with the coefficient for frequency m given by

$$\hat{s}(m) = \begin{cases} \frac{1}{2|m|} \left(\frac{r_c}{R}\right)^{|m|}, & m \neq 0 \\ \log R, & m = 0 \end{cases} \quad (\text{Laplace}),$$

$$\hat{s}(m) = \frac{i\pi}{2} H_m^{(1)}(\omega R) J_m(\omega r_c) \quad (\text{Helmholtz}). \quad (3.4)$$

Let us assume for now that $\hat{s}(m)$ never vanishes. Since u is a regular solution to the PDE, it has a (scaled) local expansion in polar coordinates

$$u(r, \theta) = \sum_{n \in \mathbb{Z}} a_n \frac{f_n(r)}{f_n(r_c)} e^{in\theta}, \quad \text{where } f_n(r) := r^{|n|} \quad (\text{Laplace}), \quad \text{or}$$

$$f_n(r) := J_n(\omega r) \quad (\text{Helmholtz}), \quad (3.5)$$

where a_n are the Fourier coefficients of u as a function of θ on the check circle (we assume that $f_n(r_c)$ never vanishes). Note that asymptotically, $f_n(r)/f_n(r_c) \sim (r/r_c)^{|n|}$ as $n \rightarrow \infty$; in the Helmholtz case, this follows from the large-order asymptotic behavior of the Bessel function [44, 10.19.1]. Since u is regular in the closed disc of radius ρ , each Fourier coefficient at radius ρ , namely $a_n f_n(\rho)/f_n(r_c)$, must be bounded, proving that

$$a_n = \mathcal{O} \left(\left(\frac{r_c}{\rho} \right)^{|n|} \right), \quad n \rightarrow \infty. \quad (3.6)$$

By orthogonality of Fourier modes on the check circle, the set of ψ_n that minimizes (3.2) is that which matches the coefficients a_n for $n \in [-n_p/2, n_p/2]$, namely

$$\psi_n = \frac{a_n}{\hat{s}(n)}, \quad n \in [-n_p/2, n_p/2].$$

The error function $u - \hat{u}$ is the remaining terms of the series for u , (3.5) so that, extrapolating this expansion into the evaluation disc we obtain,

$$\begin{aligned}
e(r) &= \sup_{s \leq r, 0 \leq \theta < 2\pi} \left| \sum_{n \notin [-n_p/2, n_p/2]} a_n \frac{f_n(s)}{f_n(r_c)} e^{in\theta} \right| \\
&\leq \sum_{n \notin [-n_p/2, n_p/2]} \frac{|a_n|}{|f_n(r_c)|} \|f_n\|_{L^\infty([0, r])}
\end{aligned}$$

Applying the asymptotics for $f_n(r)$ and (3.6), and bounding the geometric series by a constant times their first term gives

$$e(r) \leq C \left(\frac{r}{\rho} \right)^{n_p/2} \quad (3.7)$$

for some constant C independent of n_p . This error estimate for the model example matches the large- R case in the theorem below, where the proxy points are distant enough to give an accurate quadrature approximation to the above set of layer potential modes.

We now return to the general case, where we will see that when R is sufficiently close, a different type of error—aliasing or quadrature error—will instead dominate.

Remark 3.1 The analysis in this section builds upon the literature on the method of fundamental solutions (MFS). The original result for the Laplace equation is due to Katsurada [34, Theorem 2.2], who considered the case $n_c = n_p$ and restricted to $r = r_c$. We extend this result to include extrapolation from the check radius r_c out to larger radii r , and to include the Helmholtz equation.

Theorem 3.2 *Let u , the solution of the Laplace or Helmholtz Dirichlet problem on the domain Ω , be continuable as a regular solution to the Laplace or Helmholtz equation in the closed disc of radius ρ centered at \mathbf{c} . Let $R \neq 1$ in the Laplace case. Let $J_n(\omega r_c) \neq 0$, $\forall n \in \mathbb{Z}$, in the Helmholtz case (the check circle is non-resonant for Dirichlet boundary data). Let the n_p equivalent density values at proxy points be solved in exact arithmetic in the least-squares sense on the check circle as in Eq. (3.2), where \hat{u} is the expansion in Eq. (2.4). Then the error e in the disc of radius r around \mathbf{c} , as defined by Eq. (3.3), converges exponentially at the following rates,*

$$e(r) \leq \begin{cases} C \left(\frac{r}{\rho} \right)^{n_p/2}, & \rho r < R^2, \\ C n_p \left(\frac{r}{R} \right)^{n_p}, & \rho r = R^2, \\ C \left(\frac{r}{R} \right)^{n_p}, & \rho r > R^2, \end{cases} \quad (3.8)$$

where in each case, C indicates a constant that may depend on u (and therefore ω in the Helmholtz case), r , and R , but not on n_p .

Proof Our proof follows the argument in Barnett and Betcke [6, Theorem 3], with the following extensions: no assumptions are made on the check radius r_c other than $r_c < \delta$, the evaluation radius r can differ from unity, the sup norm of the solution is assumed to be bounded in the evaluation disk, rather than just being L^2 on its boundary, and the Laplace case is included.

A new aspect of the proof is that the quantity we minimize is no longer the one we bound, so that merely exhibiting a vector does not give an upper bound on the least-squares error as in [6, Theorem 3], and additional arguments are needed.

We use C and c to denote constants that are independent of n_p . We exploit (3.5) and (3.6), noting that in the case where B_r^c lies partially outside Ω , one may continue u as a regular PDE solution in the disc and these still hold (in our implementation, B_r^c at most touches the boundary, but the estimates of the theorem apply in a more general case).

By the hypotheses of the theorem, $\hat{s}(m)$ defined by (3.4) never vanishes, so, as in [6], there are constants c and C such that

$$c \frac{1}{|m|} \left(\frac{R}{r_c} \right)^{-|m|} \leq \hat{s}(m) \leq C \frac{1}{|m|} \left(\frac{R}{r_c} \right)^{-|m|}, \quad \forall m \in \mathbb{Z}. \quad (3.9)$$

The hypotheses also guarantee that $f_n(r_c)$ never vanishes, so that (3.5) is well-defined.

The proxy representation \hat{u} given by Eq. (2.4) also has an expansion of the form (3.5); let \hat{a}_n denote its coefficients. Then from [6, Eqs. (19–20)] we have

$$\hat{a}_n = \frac{n_p}{2\pi} \hat{s}(n) \hat{\alpha}_{n \bmod n_p}, \quad (3.10)$$

where the vector $\hat{\alpha} \in \mathbb{C}^{n_p}$ is the discrete Fourier transform (DFT) of the weight vector α , obtained by solving the \bmod folds integers into the range $[-n_p/2, n_p/2]$.

The squared error L^2 -norm on the check circle is then, using (3.10), proportional to

$$\sum_{n \in \mathbb{Z}} |\hat{a}_n - a_n|^2 = \sum_{n \in \mathbb{Z}} |(n_p/2\pi) \hat{s}(n) \hat{\alpha}_{n \bmod N} - a_n|^2.$$

In Fourier domain, least-squares computation of α decouples into n_p independent least-squares problems, one for each DFT coefficient $\hat{\alpha}_m, m \in [-n_p/2, n_p/2]$. Writing $n = m + bn_p$, the m th such problem is to minimize over the single number $\hat{\alpha}_m$, the quantity

$$\sum_{b \in \mathbb{Z}} |(n_p/2\pi) \hat{s}(m + bn_p) \hat{\alpha}_m - a_{m+bn_p}|^2$$

The analytic solution is

$$\begin{aligned} \hat{\alpha}_m &= \frac{\sum_{b \in \mathbb{Z}} (n_p/2\pi) \hat{s}(m + bn_p)^* a_{m+bn_p}}{\sum_{b \in \mathbb{Z}} (n_p/2\pi)^2 |\hat{s}(m + bn_p)|^2} \\ &= \frac{2\pi}{n_p} \frac{a_m}{\hat{s}(m)} (1 + \beta_m), \quad -n_p/2 \leq m < n_p/2, \end{aligned} \quad (3.11)$$

where the leading term is due to the terms $b = 0$ in the numerator and denominator sums, and the small relative correction β_m is due to the terms $b \neq 0$. Applying (3.9)

and (3.6) with $r_c < R$ and $r_c < \rho$, and bounding the geometric sums by a constant times the leading term, yields an estimate for β_m :

$$|\beta_m| \leq C \left(\frac{r_c^2}{R \min(R, \rho)} \right)^{n_p - 2|m|}, \quad -n_p/2 \leq m < n_p/2, \quad (3.12)$$

for some constant C . This means that β_m is very small apart from at the extreme frequencies $|m| \approx n_p/2$.

Similarly to the model case, the error (3.3) is then, applying (3.10) and the asymptotics of f_n ,

$$\begin{aligned} e(r) &= \sup_{s \leq r, 0 \leq \theta < 2\pi} \left| \sum_{n \in \mathbb{Z}} (\hat{a}_n - a_n) \frac{f_n(s)}{f_n(r_c)} e^{in\theta} \right| \\ &\leq \sum_{n \in \mathbb{Z}} |\hat{a}_n - a_n| \frac{\|f_n\|_{L^\infty([0, r])}}{|f_n(r_c)|} \leq C \sum_{n \in \mathbb{Z}} |(n_p/2\pi) \hat{s}(n) \hat{\alpha}_{n \bmod N} - a_n| \left(\frac{r}{r_c} \right)^{|n|}, \end{aligned}$$

where we can now substitute (3.11) for $\hat{\alpha}_n$.

For the frequencies $-n_p/2 \leq m < n_p/2$, the leading terms in (3.11) match a_n , leaving just β_m contributions there. Outside this frequency range we use that β_m is bounded and estimate the series outside the $-n_p/2 \leq m < n_p/2$ range. This leaves, applying the triangle inequality,

$$\begin{aligned} e(r) &\leq C \sum_{n \in [-n_p/2, n_p/2)} |a_n \beta_n| \left(\frac{r}{r_c} \right)^{|n|} + C \sum_{n \notin [-n_p/2, n_p/2)} \left| \hat{s}(n) \frac{a_{n \bmod n_p}}{\hat{s}(n \bmod n_p)} \right| \left(\frac{r}{r_c} \right)^{|n|} \\ &\quad + C \sum_{n \notin [-n_p/2, n_p/2)} |a_n| \left(\frac{r}{r_c} \right)^{|n|} =: E_\beta + E_u + E_v, \end{aligned}$$

where similar notation as in [6] is used for the two tail terms. The third term is easy to bound, inserting (3.6) and bounding the decaying geometric series by a constant times its leading term,

$$E_v \leq C \left(\frac{r}{\rho} \right)^{n_p/2},$$

giving the same as (3.7). The estimate for first term E_β needs (3.6) and (3.12), giving (in both cases, $R < \rho$ and $R \geq \rho$) a growing geometric sum which is bounded by a constant times its last term, $m = n_p/2$, giving (after cancellations) exactly the same order bound as E_v .

We now turn to the middle term E_u . Rewriting the sum using $n = m + bn_p$, then applying upper and lower bounds in (3.9), and (3.6) gives

$$\begin{aligned} E_u &= C \sum_{m \in [-n_p/2, n_p/2]} \left| \frac{a_m}{\hat{s}(m)} \right| \sum_{b \neq 0} |\hat{s}(m + bn_p)| \left(\frac{r}{r_c} \right)^{|m+bn_p|} \\ &\leq C \sum_{m \in [-n_p/2, n_p/2]} \left(\frac{R}{\rho} \right)^{|m|} \sum_{b \neq 0} \left(\frac{r}{R} \right)^{|m+bn_p|}. \end{aligned}$$

Notice that, as before, r_c has canceled. The b sum is decaying so can be estimated by $C(r/R)^{n_p - |m|}$. Thus

$$E_u \leq C \left(\frac{r}{R} \right)^{n_p} \sum_{m \in [-n_p/2, n_p/2]} \left(\frac{R^2}{\rho r} \right)^{|m|}.$$

There are three possibilities, giving the three cases in Eq. (3.8). If $\rho r < R^2$ the sum is geometrically growing, so can be bounded by a constant times the final term $(R^2/\rho r)^{n_p/2}$, in which case E_u dominates the other two terms, giving the first case in Eq. (3.8). If $\rho r = R^2$ there are N equal terms, and E_u still dominates, giving the second case. If $\rho r > R^2$, the sum is decaying, so is no more than a constant times its first term, simplifying to $E_u \leq C(r/\rho)^{n_p/2}$, which is the same order as E_β and E_v , giving the final case. \square

As in (3.7), r_c will not appear in Eq. (3.8), because in exact arithmetic it matters little (modulo a non-resonance condition) at what radius in $(0, R)$ the Fourier coefficients are matched. In the next section we will see that in practice rounding error strongly affects the choice of r_c , since the extrapolation is ill-conditioned. Note that the Helmholtz non-resonance condition on r_c is guaranteed if $\omega r_c < 2.4$, since all positive roots of all J -Bessel functions exceed this value; this will anyway be necessary in practice if high accuracy is needed.

A surprising aspect of Theorem 3.2 is that u may have singularities *closer* to the center than the proxy radius R and yet exponential convergence still holds; this is closely related to the Runge approximation theorem.

Remark 3.2 The two regimes in Eq. (3.8) may be interpreted as follows:

- $r < \frac{R^2}{\rho}$: the solution u is relatively rough (has a nearby singularity), and error is controlled by the decay of the local expansion coefficients a_n of u for orders beyond $n_p/2$, as in the preceding toy model.
- $r > \frac{R^2}{\rho}$: the solution u is smooth, and error is controlled instead by aliasing (in Fourier coefficient space) due to the discreteness of the proxy point representation on the proxy circle.

We observe in numerical experiments that when the boundary is adaptively refined based on the boundary data as in Sect. 2, $L \approx \rho$ and the expansion centers that dominate the error in a domain are typically those that are near to a singularity of the

solution. In our numerical experiments, when the location of singularity is known, we observed that such centers are typically in the rough regime.

Note that the boundary Γ may intersect the closed disc, and yet u may still be continued as a PDE solution into the closed disc. This requires the boundary data f or density to be analytic—see [5] for related analysis of QBX in this case.

Remark 3.3 (Extension of analysis to other kernels) It is clearly of interest to have a kernel-independent extension of Theorem 3.2 that would apply also to vector PDEs such as Stokes. Initial attempts suggest this requires significantly more complicated analysis, since to use the method of the above proof one needs to be able to write down a proxy coefficient vector α that produces a single Fourier mode on the check circle plus exponentially decaying amounts of aliased modes, which is challenging even in the Stokes case. We leave this for future work.

3.3 Modeling the effect of finite-precision arithmetic

Independence from r_c in Theorem 3.2 relies on exact arithmetic; since the extrapolation from r_c to a larger r is ill-conditioned. Moreover, due to finite precision, there are possibly fewer than n_p functions available to cancel the Fourier coefficients. As a result, we need to study the effect of rounding error on $\hat{u} - u$. Rather than attempting a rigorous analysis, we present a heuristic model and demonstrate that it agrees well with numerical observations.

For the Laplace kernel, the n th singular value of the matrix Q in Eq. (2.2) decays as $\sigma_n = \frac{1}{n}(r_c/R)^{n/2}$, i.e., marginally faster than exponentially. In the continuous limit ($n_p, n_c \rightarrow \infty$), this follows from the single-layer operator eigenvalues (3.4). The formula (3.6) shows that finite n_p introduces only an exponentially small correction. Although we do not give details, a similar argument (but with two vector components) could be made for the Stokes kernel, so that n th singular value of matrix Q corresponds to the eigenvalue for frequency $n/4$. The Helmholtz case—although there are $\mathcal{O}(\omega)$ eigenvalues that do not decay—is asymptotically identical to Laplace, as (3.9) shows; also see [6, Equation (14)]. To verify this asymptotic behavior, in Fig. 4 we show the decay of singular values for several kernels.

When the pseudoinverse of Q is computed based on Eq. (2.5), only k singular values lying above $\varepsilon_{\text{pinv}}\sigma_1$ are retained. The corresponding singular vectors approximate the lowest Fourier modes up to frequency $|n| < k/2$ (in the scalar PDE cases). Thus, equating up to constants the k th singular value above to $\varepsilon_{\text{pinv}}$, the ranks of the matrices in the pseudoinverse are

$$k \approx \min(k_m, n_p), \quad k_m = 2 \frac{\log(1/\varepsilon_{\text{pinv}})}{\log(R/r_c)}, \quad (3.13)$$

and the highest (Nyquist) frequency they can represent is $k/2$.

The values of \tilde{u} at the check points have error bounded by e_c , so in this model we expect the errors to be amplified (by considering the local expansion as above) to become $e_c(r/r_c)^{k/2}$ at the evaluation radius r .

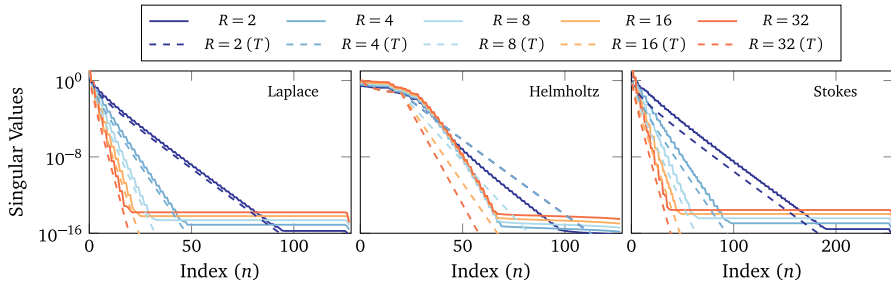


Fig. 4 Singular values of proxy to check matrix. The solid lines are the singular values of Q for different R and different single-layer kernels, and the dashed lines labeled (T) are the theoretical decay: $\frac{1}{n}(r_c/R)^{n/2}$ for Laplace or Helmholtz, and $\frac{1}{n}(r_c/R)^{n/4}$ for Stokes, where n denotes the index of the singular value. Other parameters are $r_c = 1$, $n_p = 128$, $n_c = 256$. For the Helmholtz problem, the dashed lines show the asymptotic bound for the singular values and are not accurate for small indices; the interested reader is referred to [6, Eq. (14)]

3.4 Error bounds and choice of parameters

Combining the rigorous results from Sect. 3.2 with the heuristic of Sect. 3.3 for a kernel-independent expansion, using n_p proxy points, the error in the scalar PDE cases is approximately bounded by

$$e(r) \leq \begin{cases} C \left(\frac{r}{\rho} \right)^{k/2} + C e_c \left(\frac{r}{r_c} \right)^{k/2}, & \rho r < R^2, \\ C \left(\frac{r}{R} \right)^{n_p} + C e_c \left(\frac{r}{r_c} \right)^{k/2}, & \rho r > R^2, \end{cases} \quad (3.14)$$

where C represents possibly different constants in each case (omitting the case $\rho r = R^2$).

In Fig. 5, we show how this formula models the error growth for a single kernel-independent expansion interpolating a Laplace solution in free space with a known nearest singularity at various distances ρ , for a typical choice of ratio $R/r_c = 8$. The key observation is that, despite its simplicity, our model Eq. (3.14) explains well the observed error behavior. Other salient features of the plots include:

- As r increases beyond r_c , errors grow rapidly dominated by the second term in the error estimate.
- The error is mostly controlled by k and increasing n_p beyond $k_m \approx 27$ (defined in Eq. 3.13) has no tangible effect unless $\rho r > R^2$ (i.e., right half of leftmost plot in Fig. 5).

Figure 6 instead continuously varies R/ρ (the inverse scaled singularity distance), showing the same effect: a relatively distant singularity allows high accuracy expansion out to larger r/R .

Choice of parameters Using the model Eq. (3.14), one can make choices for R , r_c , δ , and n_p to achieve a desired accuracy ε . An unknown in applying this in a practical

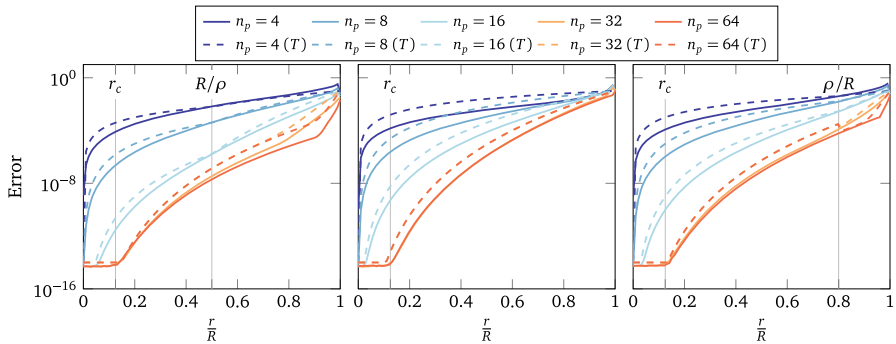


Fig. 5 Error bounds for Laplace QBKIX with known singularity. Errors e observed (solid lines) and predicted by Eq. (3.14) (dashed lines) for a single expansion with different singularity distances $\rho = 2R$, R , and $0.8R$, and different numbers of proxy points n_p . The expansion is centered at $\mathbf{c} = [0, 0]$ and the solution $u(\mathbf{x}) = -\log |\mathbf{x} - \mathbf{x}_0|$, $\mathbf{x}_0 = \rho e^{1i/19}$ is a harmonic function with a singularity at distance ρ . Laplace single-layer kernel is used for the expansion. The error is the maximum error over the B_r^c as defined in Eq. (3.3). The proxy to check radius ratio is $R/r_c = 8$, the number of checks is set to $n_c = 2n_p$, $e_c = 10^{-14}$, and $k_m \approx 27$ [given by Eq. (3.13) with $\varepsilon_{\text{pinv}} = 10^{-14}$]. The constants C in Eq. (3.14) were chosen to qualitatively match the trend lines (all set to 0.1)

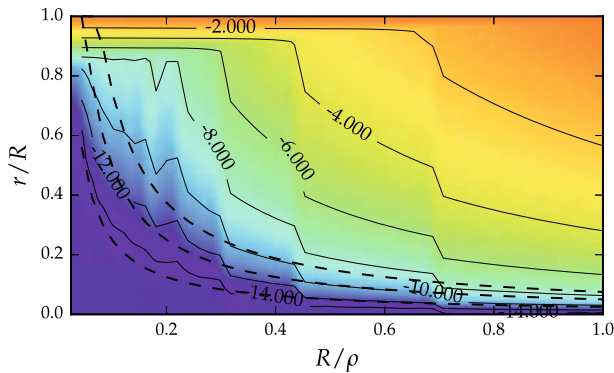


Fig. 6 Error at different evaluation radii. The error for evaluation of a single expansion with various R and r , but fixed $r_c = \rho/40$ and ρ . The expansion is interpolating a harmonic function (similar to the one used in Fig. 5) with singularity at distance $\rho = 4$, using the Laplace double-layer kernel. The dotted lines are $r = mr_c$ for $m = 1, 2$, and 3 . In practice, we have no direct control on $\frac{R}{\rho}$, and it is implied by the panel size. Here we chose $n_p = 64$, and $n_c = 2n_p$; the trends are the same for lower n_p and n_c

setting is the singularity distance ρ . However, in any high-accuracy choice of boundary quadrature, such as the adaptive panel quadrature of Sect. 2, panels are refined such that the data f and hence the density ϕ and the solution u are smooth on the local panel scale L , thus we expect singularities to be at least of order L distant from the center. Indeed, we experimentally observe (in tests where we know the location of singularity, e.g., Fig. 7 or Sect. 4.3) that when the panels are adaptively refined, $L < \rho$, and consequently the convergence behavior is most like the left-hand plot of Fig. 5.

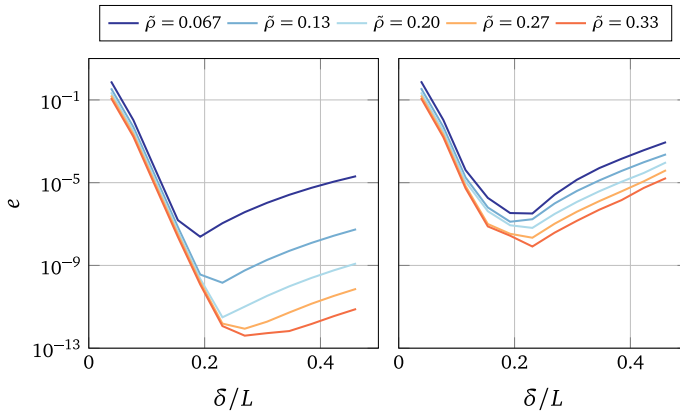


Fig. 7 Error versus center and singularity distances. The induced error for singularities and centers at various distances from the boundary for the Laplace Dirichlet interior BVP, in the domain shown in Fig. 9. The boundary data is generated by putting a Laplace singularity at distance $\tilde{\rho}$ from the boundary—the singularity distance to the center of expansion is $\rho \geq \tilde{\rho} + \delta$. The density is solved directly and QBKIX is used only for evaluation. The error is computed using the known solution corresponding to the boundary data. The left plot shows the errors for the case with fixed number of panels on the boundary ($M = 40$ panels). In this plot, because L is fixed, $L/\tilde{\rho}$ is decreasing by increasing $\tilde{\rho}$. The right plot shows the errors for adaptive refinement of the boundary with $\varepsilon_a = 10^{-11}$. Here, since L is chosen adaptively due to the boundary data, it increases as the solution becomes smoother. Because, L is chosen proportional to $\tilde{\rho}$, the error curves almost collapse to one. We use $n_p = 64$, $n_c = 2n_p$, $r_c = \delta/3$ and $R = 8r_c$. In both cases, the center of expansion is located based on the panel size at distance δ

Given the target accuracy of ε for the solution and the selected smooth quadrature order q , the adaptive refinement of boundary sets the panel length L . We use the following steps to glean the value of other parameters. Since the constants in the error estimates are problem dependent and unknown, we set them to unity. To have a concrete example, we pick $\varepsilon = 10^{-10}$ and $q = 16$.

- (1) **Setting δ :** By construction, points farther than 2δ from the boundary are evaluated using the smooth quadrature. To meet the desired error ε at these points, $\frac{L}{\delta} \approx 8\varepsilon^{1/2q}$, which implies $\delta \approx L/4$ for $\varepsilon = 10^{-10}$, $q = 16$.
- (2) **Setting k_m , R/r_c , and n_p :** Requiring that the two terms in the error estimate (i.e., proxy point representation and extrapolation errors) have similar contribution at the on surface point ($r = \delta$) and assuming that $L \approx \rho$ we can estimate the minimum required k based on the proxy representation error in the rough regime:

$$\left(\frac{\delta}{\rho}\right)^{k/2} \approx \varepsilon \quad \text{or} \quad k \approx \frac{2 \log \varepsilon}{\log (\delta/L)}, \quad (3.15)$$

implying $k \approx 32$ for $L/\delta = 4$, $\varepsilon = 10^{-10}$. Since k is bounded by $\min(k_m, n_p)$, knowing minimum k implies a lower bound for k_m and n_p . Therefore, reorganizing Eq. (3.13), we have $R/r_c = \varepsilon_{\text{pinv}}^{2/k} \approx 7$, for $\varepsilon_{\text{pinv}} = 10^{-14}$.

- (3) **Setting r_c/δ and β :** Inspecting the extrapolation error at an on surface point, we have

$$e_e(\delta) \approx e_c \left(\frac{\delta}{r_c} \right)^{k/2} \approx \left(\frac{L}{4\beta(\delta - r_c)} \right)^{2q} \left(\frac{\delta}{r_c} \right)^{k/2} \approx \left(\frac{L}{4\beta\delta} \right)^{2q} \frac{1}{(1-\theta)^{2q}\theta^{k/2}}, \quad (3.16)$$

where $\theta = r_c/\delta$. This expression attains its minimum at $\theta = \frac{k}{4q+k}$. For $q = 16$ and $k = 32$, we have $\theta = 1/3$. As we require that two terms in the error estimate have similar contribution, we use $e_e(\delta)$ and estimate β :

$$\beta \approx \frac{L/4\delta}{(1-\theta)\theta^{k/4q}\varepsilon^{1/2q}}, \quad (3.17)$$

implying $\beta = 5$, for the choices of parameter listed above.

Note that we have not analyzed the effect of finite n_c , but find that the choice $n_c = 2n_p$ behaves indistinguishably from the limit $n_c \rightarrow \infty$; we attribute this to the rapid convergence of the periodic trapezoid rule on the check points.

4 Numerical experiments

In this section, we present the results of numerical tests demonstrating the accuracy and versatility of the QBKIX algorithm for on-surface evaluation needed for the boundary integral equation solver and solution evaluation close to the surface. In the following experiments, unless noted otherwise, we use QBKIX for both tasks.

4.1 Convergence with respect to the number of panels

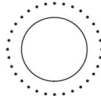
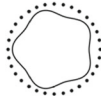
In Table 1, we report the error in the evaluation of single- and double-layer potentials at a set of points on the boundary by verifying Green's identity for a known function u . The test solution u is constructed by putting singularities with random strength at points marked outside the domain. The Dirichlet and Neumann data for this solution is evaluated on the boundary and QBKIX is used to evaluate the layer potential on boundary points. The error is

$$e_g(\mathbf{x}) = \left| \mathcal{S} \left[\frac{\partial u}{\partial \mathbf{n}} \right] (\mathbf{x}) - \mathcal{D}[u](\mathbf{x}) - u(\mathbf{x}) \right|,$$

where \mathcal{S} and \mathcal{D} denote single- and double- layer operators that are evaluated using one-sided QBKIX. We have chosen simple geometries such that all panels are nearly-admissible (to observe convergence trend, they need to violate the first condition). For all cases, QBKIX achieves high-order convergence rate, albeit lower accuracy for Stokes and elastostatic kernels.




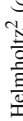
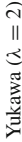
In Table 2, we report the convergence of the solution evaluated at the interior points using non-adaptive boundary quadrature with increasing number of panels. The test solution is the potential due to a set of singularities at the source points shown outside the domain. These source points are used to generate the boundary data f

Table 1 Error in Green's identity versus number of panels

Geometry	PDE	Absolute error (Number of panels)				
	Laplace	$3.83e-04$ (2)	$3.06e-06$ (4)	$1.04e-07$ (6)	$6.27e-09$ (8)	$8.88e-10$ (10)
	Yukawa ($\lambda = 2$)	$3.40e-04$ (2)	$2.98e-06$ (4)	$1.03e-07$ (6)	$6.28e-09$ (8)	$8.61e-10$ (10)
	Helmholtz ($\omega = 2$)	$3.19e-04$ (2)	$2.91e-06$ (4)	$1.04e-07$ (6)	$8.47e-09$ (8)	$8.48e-10$ (10)
	Stokes	$2.03e-02$ (2)	$5.64e-04$ (4)	$4.45e-05$ (6)	$2.47e-06$ (8)	$1.27e-07$ (10)
	Elastostatic ($\nu = 0.1$)	$1.90e-03$ (2)	$3.85e-05$ (4)	$2.43e-06$ (6)	$1.46e-07$ (8)	$7.57e-09$ (10)
	Laplace	$1.39e-03$ (6)	$8.97e-06$ (12)	$4.11e-07$ (18)	$3.57e-08$ (24)	$4.36e-09$ (30)
	Yukawa ($\lambda = 2$)	$1.27e-03$ (6)	$7.13e-06$ (12)	$4.12e-07$ (18)	$3.58e-08$ (24)	$4.41e-09$ (30)
	Helmholtz ($\omega = 2$)	$1.37e-03$ (6)	$8.99e-06$ (12)	$4.13e-07$ (18)	$3.57e-08$ (24)	$4.33e-09$ (30)
	Stokes	$4.18e-03$ (6)	$6.67e-05$ (12)	$6.17e-06$ (18)	$4.65e-07$ (24)	$5.52e-08$ (30)
	Elastostatic ($\nu = 0.1$)	$3.46e-02$ (6)	$1.24e-03$ (12)	$8.73e-05$ (18)	$7.90e-06$ (24)	$8.86e-07$ (30)

Verifying Green's identity for a known function constructed by putting singularities with random strength at points marked outside the domain. The Dirichlet and Neumann data for this solution is evaluated on the boundary and QBKIX is used to evaluate the layer potential on boundary points

Table 2 Solution convergence versus number of panels

Geometry	Kernel	Quadrature	Absolute error (Number of panels)
	Laplace	Direct	2.90e-06 (2) 9.46e-10 (4) 6.42e-14 (6) 1.98e-14 (8)
		QBKIX (one)	3.39e-06 (2) 9.69e-10 (4) 4.46e-12 (6) 3.54e-12 (8)
		QBKIX (two)	2.25e-05 (2) 4.07e-07 (4) 2.24e-08 (6) 2.37e-09 (8)
	Laplace	Direct	5.80e-07 (6) 8.52e-07 (8) 1.67e-09 (10) 5.65e-12 (12)
		QBKIX (one)	2.49e+00 (6) ¹ 1.32e-04 (8) 4.62e-09 (10) 3.09e-09 (12)
		QBKIX (two)	4.29e-01 (6) 3.06e-04 (8) 4.25e-07 (10) 1.50e-07 (12)
	Stokes	Direct	1.48e-04 (6) 6.67e-05 (8) 6.51e-08 (10) 6.06e-10 (12)
		QBKIX (one)	2.89e-08 (20) 4.78e-09 (24) 1.73e-09 (28) 6.38e-10 (32)
		QBKIX (two)	6.95e-06 (16) 4.87e-08 (32) 3.31e-09 (48) 9.45e-10 (64)
	Helmholtz ² ($\omega = 2$)	QBKIX (one)	2.12e-04 (8) 1.20e-09 (12) 4.22e-10 (16) 2.09e-11 (20)
		QBKIX (two)	3.97e-04 (8) 1.91e-07 (12) 3.42e-08 (16) 7.92e-09 (20)
		QBKIX (one)	1.60e-04 (8) 6.42e-07 (12) 3.84e-09 (16) 1.48e-09 (20)
	Yukawa ($\lambda = 2$)	QBKIX (two)	5.44e-04 (8) 1.27e-07 (12) 2.19e-08 (16) 4.79e-09 (20)
		QBKIX (one)	2.07e-03 (8) 7.16e-06 (12) 4.35e-07 (16) 7.19e-07 (20)
		QBKIX (two)	3.17e-02 (8) 1.27e-05 (12) 2.26e-06 (16) 6.77e-07 (20)

Error in the solution to interior Dirichlet boundary value problems using non-adaptive M -panel quadrature and QBKIX for solution. The subplots show Γ (solid) and the exterior sources used to generate the solution, and interior test points. There are 40 source points outside the domain and error is measured on 40 points inside. The error is the maximum of absolute error over these interior points. The numerical parameters are $n_p = 32$, $n_c = 2n_p$, $R = 8r_c$, and $\delta = 3r_c$. “Direct” indicates usage of the quadrature of Eq. (1.9) instead of QBKIX for the linear solve. “One” and “two” indicate one- or two-sided versions of on-surface QBKIX discussed in Sect. 2.2.

¹ When there are a few panels on the boundary, a check circle may be placed near other panels which adversely affects the error.

² For Helmholtz equation, we use a combined field formulation

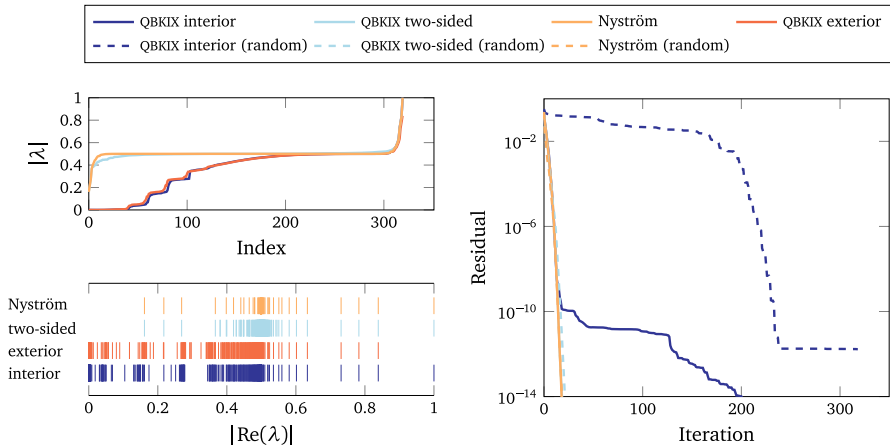


Fig. 8 The spectra of discretizations of the Laplace double-layer operator. This figure shows eigenvalues, and the GMRES convergence rate, for different discretizations of the Laplace double-layer operator in the domain shown in Fig. 9. The left plots show the real part and the magnitude of the eigenvalues corresponding the one-sided interior QBKIX, one-sided exterior QBKIX, two-sided QBKIX, and the plain Nystrom matrix. See Sects. 2.2 and 4.2. The right plot shows the residual versus the iteration number for the three interior variants with two different right hand sides (boundary data corresponding to a harmonic function or random data). The residual of the two-sided and Nystrom schemes are indistinguishable

and the reference solution to check the error. For all problems, the double-layer formulation is used, except for the Helmholtz for which a combined-field formulation $u = \mathcal{D}[\phi] + i\omega\mathcal{S}[\phi]$, where \mathcal{S} is the single-layer potential [16, Section 3.2], is used. This representation addresses problems associated with resonance of the complementary domain. The double-layer (or combined-field) density ϕ is solved using QBKIX to evaluate the matrix-vector product in each iteration of GMRES. The error in the density is quantified by computing the solution from ϕ , Eq. (1.5), at a set of target points in the interior of the domain. For the first three kernels, which are smooth, we also report the convergence using the Nystrom (*direct*) evaluation, Eq. (1.9), which by comparison against one- or two-sided QBKIX shows how much of the error is due to QBKIX.

In all cases, it can be seen that QBKIX gives high-order convergence rate that is independent of the type of the kernel. We notice that the error performance of the two-sided variant is worse than one-sided at the same number of panels (however, as we discuss below, it is valuable since it improves the convergence rate of GMRES).

4.2 Operator spectrum and GMRES convergence rate

We now perform numerical tests of the one-sided and two-sided variants of on-surface evaluation of QBKIX discussed in Sect. 2.2 and compare it to direct use of an accurate quadrature. To simplify comparisons, we use an operator with a smooth kernel (Laplace). The spectra and convergence behavior for singular kernels is similar. In Fig. 8 we plot—for the domain shown in Fig. 9 and the Laplace equation—the eigen-

values for four different approximations to the operator $-\frac{1}{2} + D$: one-sided (interior) QBKIX, the one-sided (exterior) QBKIX, two-sided QBKIX, and the quadrature given by Eq. (1.9), to which we refer as *direct*. The exterior version of QBKIX is constructed similarly to the interior variant discussed in Sect. 2. The only modification is that for each collocation point \mathbf{x}_0 on Γ , we place an expansion center at $\mathbf{c} = \mathbf{x}_0 + \delta \mathbf{n}$. We see that the one-sided variants have clusters of eigenvalues near zero, whereas the two-sided variant and the Nyström matrix have a cleaner spectrum with eigenvalue clustering only around $\frac{1}{2}$.

A broader spread of the eigenvalues has a negative impact on GMRES convergence [42]. Figure 8, right, shows GMRES residual versus the iteration number for the interior, two-sided, and direct operators with two different right-hand sides (boundary data corresponding to a harmonic function and a random right-hand side).

The convergence of one-sided interior QBKIX is identical to the Nyström method convergence up to the residual magnitude on the order of numerical accuracy of QBKIX, but it slows down once the residual decreases below this value (near 10^{-9}). The two-sided variant has identical convergence behavior to the direct method, and converges in a few iterations. We also show the residual for a random-right hand side to expose the effect of near-zero eigenvalues: we see that convergence is very slow for the one-sided scheme in this case, but for the two-sided scheme it is the same as for the true smooth data f .

4.3 Error for Dirichlet problems for five PDEs

For this set of tests, we use adaptive refinement as described in Sect. 2. We use QBKIX both as the on-surface quadrature scheme when solving for the desired density as well as the evaluator for the near-singular integrals. As before, we use boundary data sampled from a sum of fundamental solutions centered at a set of points close to the boundary. Figure 9 plots the error across the domain for all of the PDEs listed in Eq. (1.4), on the points lying on a 600×600 grid and interior to the domain. When an evaluation point is within 2δ distance from the boundary, it is evaluated using the nearest QBKIX expansion. The remaining points are evaluated using Eq. (1.7) applied to Eq. (1.5).

We observe that parameter choices which were selected for the Laplace equation perform well for the other PDEs. As expected, the highest error is due to expansions for panels adjacent to larger ones (e.g. Fig. 9a).

4.4 Domain with a large number of corners

As a final example, we use QBKIX in a domain with 256 corners as shown in Fig. 10. A Laplace boundary value problem is solved using GMRES with tolerance for relative residual set to $\varepsilon_r = 10^{-6}$. The boundary condition is generated by placing source points at locations marked by dots outside the domain in Fig. 10b. The strength of the each source point is chosen randomly from $[-25, 25]$.

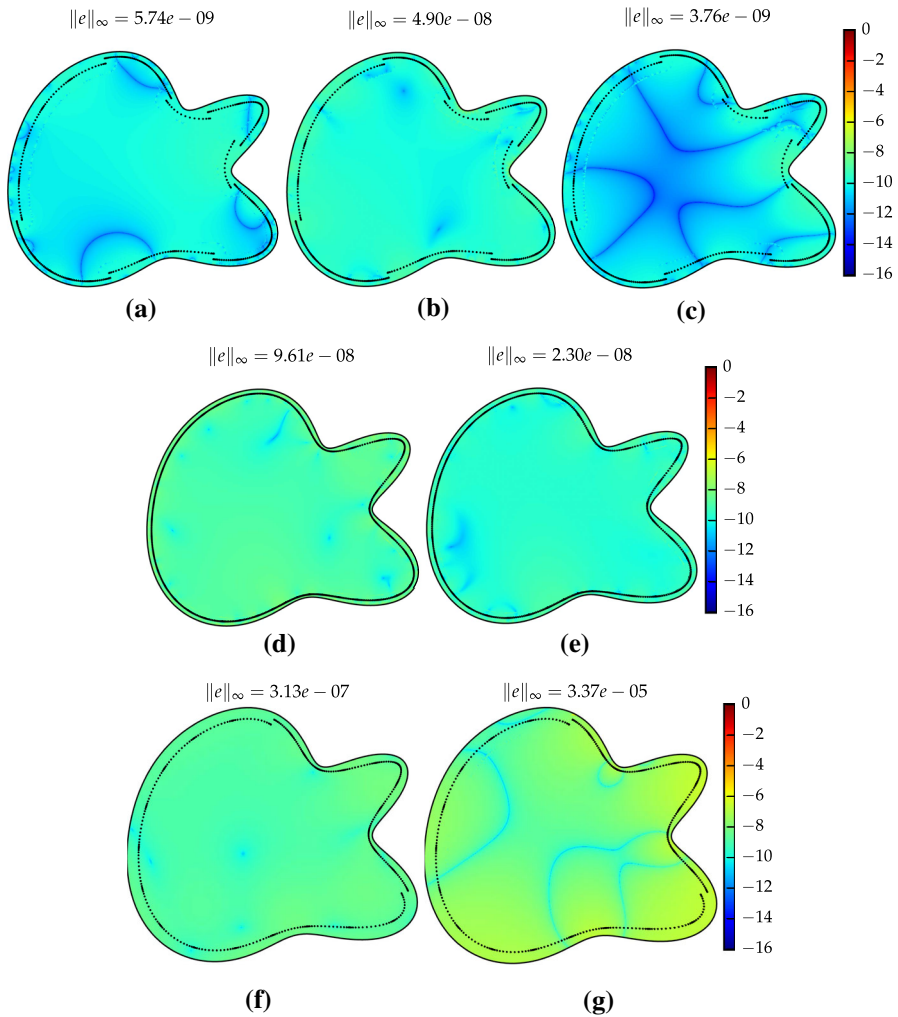


Fig. 9 The \log_{10} of pointwise error. The interior Dirichlet boundary value problem is solved with known solution generated by source points distributed over an exterior circle as shown in the lower figure in Table 2, apart from in (f) and (g) where we use the cubic flow with velocity $\mathbf{u} = [y^3, x^3]$ and pressure $p = 6xy$. Error is evaluated on the same fine grid used for visualization (600×600). We use $q = 16$ node Gauss–Legendre panels and set $\varepsilon_a = 10^{-13}$ in the adaptive panel quadrature set-up. M denotes the number of boundary panels. The expansion centers \mathbf{c} are shown by black dots close to the boundary. **a** Laplace ($M = 30$), **b** Helmholtz ($M = 30$), **c** Yukawa ($M = 30$), **d** Stokes velocity ($M = 48$), **e** Elastostatic ($M = 40$), **f** Smooth stokes velocity ($M = 26$), **g** Smooth stokes pressure ($M = 26$)

The boundary of the domain is adaptively refined, with minimum panel length set to $\varepsilon_l = \varepsilon_r/10$. Large panels are also refined based on the adaptive criterion we outlined in Sect. 2. The dyadic and adaptive refinements result in a total of 10072 panels.

Due to the singularities on the boundary, the system matrix is ill-conditioned. The ill-conditioning is greatly reduced using left and right preconditioners with square

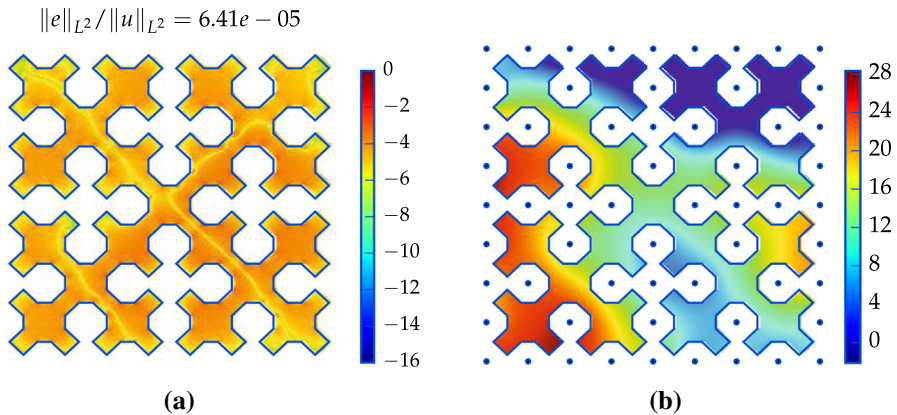


Fig. 10 QBKIX in a domain with 256 corners. Laplace Dirichlet boundary value problem. The boundary condition is generated by placing source points at locations marked by dots outside the domain in (b). The strength of the each source point is chosen randomly from $[-25, 25]$. We use a 2D composite trapezoidal rule with 600×600 points in the unit box $[0, 1] \times [0, 1]$ to compute the reported L^2 error. **a** The \log_{10} of relative pointwise error, **b** solution

root of smooth quadrature weights on its diagonal [11], solving for density in L^2 sense. Considering this preconditioning and since the last panel in each side of the corner is of length smaller than $\varepsilon_r/10$, we set the density on those panels to zero (effectively deleting the last two panels). The GMRES converges after 38 iterations; we use KIFMM (with accuracy set to $\varepsilon_r/10$) for fast evaluation.

In Fig. 10, we measure the error in the L^2 sense because both dyadic refinement of panels approaching the corners as well as the L^2 preconditioning of the system may cause the error for point closer than ε_l to a corner to be potentially large.

5 Conclusions

In this paper we introduced a new quadrature scheme for the high-order accurate evaluation of layer potentials associated with general elliptic PDE on the domain boundary and close to it. The scheme—which builds local solution approximations using a refined evaluation and the solution of small linear systems—relies solely on the evaluation of the underlying kernel, so is essentially PDE-independent. It is highly flexible, being agnostic as to the boundary condition type, the layer representation, and crucially, the dimension of the problem. We have analyzed the error behavior of the scheme for Laplace and Helmholtz cases. It also fits naturally in the framework of existing fast kernel-independent algorithms for potential evaluation such as the KIFMM, as it uses similar local approximations.

We have tested its accuracy for three scalar- and two vector-valued 2D Dirichlet boundary-value problems that are common in engineering problems. We have not attempted to optimize performance, and leave that for future work.

There are several obvious extensions that have motivated this initial study that we plan to pursue:

- (1) Generalization to 3D. High-order singular quadratures for surfaces are complicated, application dependent, and scarce. Since it requires only pointwise kernel evaluations, QBKIX is by design very easy to implement in 3D using proxy and check surfaces, and would handle a wide class of PDEs. The constants will be larger, but the linear systems (anticipated to be of size around 10^3) would still be very practical.
- (2) Application to other boundary conditions. QBX, and thus also QBKIX, can apply without modification, for instance, the normal derivative of the double-layer operator, which is hypersingular, and can occur when Neumann conditions are needed.
- (3) Integration with KIFMM. In this work, we only used kernel-independent FMM for fast evaluation of potential on the check points. However, we expect performance gains by reusing the local expansion of KIFMM as a QBKIX expansion.
- (4) Local QBKIX. The construction of local schemes which automatically handle general domains with thin features (i.e., with geodesically distant parts of the boundary in close proximity in space) without excessive refinement needed for the panel size to be on the order of feature size, is important for making the method practical. [5] proposed the *local* version of QBX, in which only the contribution of the nearby panels to a target is evaluated using expansions, while contributions of more distant panels is evaluated using standard quadrature. Implementing this idea is nontrivial however, as the end-points of the group of neighboring panels produce new singularities that can affect the convergence rate.
- (5) Generalization of analysis to all kernels. As Remark 3.3 discusses, this is a non-trivial missing piece in the theoretical foundations.

Acknowledgements We extend our thanks to Manas Rachh, Andreas Klöckner, Michael O’Neil, and Leslie Greengard for stimulating conversations about various aspects of this work. A.R. and D.Z. acknowledge the support of the US National Science Foundation (NSF) through Grant DMS-1320621; A.B. acknowledges the support of the NSF through Grant DMS-1216656.

Appendix A: List of kernels

Here we list the kernels for the single- and double-layer potentials for the PDEs considered text. In each case \mathbf{x} and \mathbf{y} are points in \mathbb{R}^2 and $\mathbf{r} := \mathbf{x} - \mathbf{y}$. The single-layer kernel is the fundamental solution. In double-layer kernels, \mathbf{n} is the unit vector denoting the dipole direction, which in the context of boundary integral formulation is the outward pointing normal to the surface.

- Laplace:

$$\Delta u = 0, \quad (\text{A.1})$$

$$S(\mathbf{x}, \mathbf{y}) = -\frac{1}{2\pi} \log |\mathbf{r}|, \quad (\text{A.2})$$

$$D(\mathbf{x}, \mathbf{y}) = \frac{1}{2\pi} \frac{\mathbf{r} \cdot \mathbf{n}}{|\mathbf{r}|^2}, \quad (\text{A.3})$$

$$\lim_{\mathbf{y} \rightarrow \mathbf{x}} D(\mathbf{x}, \mathbf{y}) = -\frac{\kappa}{4\pi}, \quad \mathbf{x}, \mathbf{y} \in \Gamma, \quad (\text{where } \kappa \text{ is the signed curvature}). \quad (\text{A.4})$$

- Yukawa:

$$\Delta u - \lambda^2 u = 0, \quad (\text{A.5})$$

$$S(\mathbf{x}, \mathbf{y}) = \frac{1}{2\pi} K_0(\lambda |\mathbf{r}|), \quad (\text{A.6})$$

$$D(\mathbf{x}, \mathbf{y}) = \frac{\lambda}{2\pi} \frac{\mathbf{r} \cdot \mathbf{n}}{|\mathbf{r}|} K_1(\lambda |\mathbf{r}|), \quad (\text{A.7})$$

where K_0, K_1 are modified Bessel functions of the second kind of order zero and one, respectively.

- Helmholtz:

$$\Delta u + \omega^2 u = 0, \quad (\text{A.8})$$

$$S(\mathbf{x}, \mathbf{y}) = \frac{i}{4} H_0^1(\omega |\mathbf{r}|), \quad (\text{A.9})$$

$$D(\mathbf{x}, \mathbf{y}) = \frac{i\omega}{4} \frac{\mathbf{r} \cdot \mathbf{n}}{|\mathbf{r}|} H_1^1(\omega |\mathbf{r}|), \quad (\text{A.10})$$

where H_0^1, H_1^1 are respectively modified Hankel functions of the first kind of order zero and one.

- Stokes:

$$-\Delta \mathbf{u} + \nabla p = 0, \quad \nabla \cdot \mathbf{u} = 0, \quad (\text{A.11})$$

$$S(\mathbf{x}, \mathbf{y}) = \frac{1}{4\pi} \left(-\log |\mathbf{r}| + \frac{\mathbf{r} \otimes \mathbf{r}}{|\mathbf{r}|^2} \right), \quad (\text{A.12})$$

$$D(\mathbf{x}, \mathbf{y}) = \frac{\mathbf{r} \cdot \mathbf{n}}{\pi} \frac{\mathbf{r} \otimes \mathbf{r}}{|\mathbf{r}|^4}, \quad (\text{A.13})$$

$$\lim_{\mathbf{y} \rightarrow \mathbf{x}} D(\mathbf{x}, \mathbf{y}) = -\frac{\kappa}{2\pi} \mathbf{t} \otimes \mathbf{t}, \quad (\text{A.14})$$

$$P(\mathbf{x}, \mathbf{y}) = -\frac{1}{\pi |\mathbf{r}|^2} \left(1 - 2 \frac{\mathbf{r} \otimes \mathbf{r}}{|\mathbf{r}|^2} \right) \mathbf{n}. \quad (\text{A.15})$$

- Navier: Linear elasticity for isotropic material with shear modulus μ and Poisson ratio ν ,

$$\mu \Delta \mathbf{u} + \frac{\mu}{1-2\nu} \nabla \nabla \cdot \mathbf{u} = 0, \quad (\text{A.16})$$

$$S(\mathbf{x}, \mathbf{y}) = -\frac{3-4\nu}{8\pi(1-\nu)} \log |\mathbf{r}| + \frac{1}{8\pi(1-\nu)} \frac{\mathbf{r} \otimes \mathbf{r}}{|\mathbf{r}|^2}, \quad (\text{A.17})$$

$$D(\mathbf{x}, \mathbf{y}) = \frac{1-2\nu}{4\pi(1-\nu)} \left(\frac{\mathbf{r} \cdot \mathbf{n} + \mathbf{n} \otimes \mathbf{r} - \mathbf{r} \otimes \mathbf{n}}{|\mathbf{r}|^2} + \frac{2}{1-2\nu} \frac{\mathbf{r} \cdot \mathbf{n}}{|\mathbf{r}|^4} \mathbf{r} \otimes \mathbf{r} \right). \quad (\text{A.18})$$

References

1. af Klinteberg, L., Tornberg, A.K.: Adaptive quadrature by expansion for layer potential evaluation in two dimensions (2017). Preprint, [arXiv:1704.02219](https://arxiv.org/abs/1704.02219)
2. af Klinteberg, L., Tornberg, A.K.: Error estimation for quadrature by expansion in layer potential evaluation. *Adv. Comput. Math.* **43**(1), 195–234 (2017)
3. Alpert, B.K.: Hybrid Gauss-trapezoidal quadrature rules. *SIAM J. Sci. Comput.* **20**, 1551–1584 (1999)
4. Atkinson, K.: *The Numerical Solution of Integral Equations of the Second Kind*. Cambridge University Press, Cambridge (1997)
5. Barnett, A.H.: Evaluation of layer potentials close to the boundary for Laplace and Helmholtz problems on analytic planar domains. *SIAM J. Sci. Comput.* **36**(2), A427–A451 (2014)
6. Barnett, A.H., Betcke, T.: Stability and convergence of the method of fundamental solutions for helmholtz problems on analytic domains. *J. Comput. Phys.* **227**(14), 7003–7026 (2008)
7. Barnett, A.H., Wu, B., Veerapaneni, S.: Spectrally-accurate quadratures for evaluation of layer potentials close to the boundary for the 2D Stokes and Laplace equations. *SIAM J. Sci. Comput.* **37**(4), B519–B542 (2015)
8. Beale, J., Lai, M.C.: A method for computing nearly singular integrals. *SIAM J. Numer. Anal.* **38**, 1902–1925 (2001)
9. Beale, J.T., Ying, W., Wilson, J.R.: A simple method for computing singular or nearly singular integrals on closed surfaces. *Commun. Comput. Phys.* **20**(3), 733–753 (2016)
10. Bogomolny, A.: Fundamental solutions method for elliptic boundary value problems. *SIAM J. Numer. Anal.* **22**(4), 644–669 (1985)
11. Bremer, J.: On the nyström discretization of integral equations on planar curves with corners. *Appl. Comput. Harmon. Anal.* **32**(1), 45–64 (2012)
12. Bremer, J., Gimbutas, Z.: A Nyström method for weakly singular integral operators on surfaces. *J. Comput. Phys.* **231**, 4885–4903 (2012)
13. Bremer, J., Rokhlin, V.: Efficient discretization of Laplace boundary integral equations on polygonal domains. *J. Comput. Phys.* **229**, 2507–2525 (2010)
14. Bremer, J., Rokhlin, V., Sammis, I.: Universal quadratures for boundary integral equations on two-dimensional domains with corners. *J. Comput. Phys.* **229**(22), 8259–8280 (2010)
15. Bruno, O.P., Kunyansky, L.A.: A fast, high-order algorithm for the solution of surface scattering problems: basic implementation, tests, and applications. *J. Comput. Phys.* **169**, 80–110 (2001)
16. Colton, D., Kress, R.: *Inverse acoustic and electromagnetic scattering theory*. In *Applied Mathematical Sciences*, vol. 93, 2nd edn. Springer, Berlin (1998)
17. Corona, E., Rahimian, A., Zorin, D.: A tensor-train accelerated solver for integral equations in complex geometries. *J. Comput. Phys.* **334**, 145–169 (2017)
18. Davis, P.J., Rabinowitz, P.: *Methods of Numerical Integration*. Academic Press, San Diego (1984)
19. Duffy, M.G.: Quadrature over a pyramid or cube of integrands with a singularity at a vertex. *SIAM J. Numer. Anal.* **19**(6), 1260–1262 (1982)
20. Epstein, C.L., Greengard, L., Klöckner, A.: On the convergence of local expansions of layer potentials. *SIAM J. Numer. Anal.* **51**, 2660–2679 (2013)
21. Farina, L.: Evaluation of single layer potentials over curved surfaces. *SIAM J. Sci. Comput.* **23**(1), 81–91 (2001)
22. Ganesh, M., Graham, I.: A high-order algorithm for obstacle scattering in three dimensions. *J. Comput. Phys.* **198**(1), 211–242 (2004)
23. Graglia, R.D., Lombardi, G.: Machine precision evaluation of singular and nearly singular potential integrals by use of gauss quadrature formulas for rational functions. *IEEE Trans. Antennas Propag.* **56**(4), 981–998 (2008)
24. Graham, I., Sloan, I.: Fully discrete spectral boundary integral methods for Helmholtz problems on smooth closed surfaces in \mathbb{R}^3 . *Numer. Math.* **92**(2), 289–323 (2002)
25. Hackbusch, W., Sauter, S.A.: On numerical cubatures of nearly singular surface integrals arising in bem collocation. *Computing* **52**(2), 139–159 (1994)
26. Hao, S., Barnett, A.H., Martinsson, P.G., Young, P.: High-order accurate Nyström discretization of integral equations with weakly singular kernels on smooth curves in the plane. *Adv. Comput. Math.* **40**(1), 245–272 (2014)
27. Helsing, J.: Integral equation methods for elliptic problems with boundary conditions of mixed type. *J. Comput. Phys.* **228**, 8892–8907 (2009)

28. Helsing, J.: Solving integral equations on piecewise smooth boundaries using the RCIP method: a tutorial (2012). [arXiv:1207.6737v3](https://arxiv.org/abs/1207.6737v3)
29. Helsing, J., Ojala, R.: On the evaluation of layer potentials close to their sources. *J. Comput. Phys.* **227**, 2899–2921 (2008)
30. Hsiao, G., Wendland, W.L.: *Boundary Integral Equations*. Applied Mathematical Sciences, vol. 164. Springer, Berlin (2008)
31. Järvenpää, S., Taskinen, M., Ylä-Oijala, P.: Singularity extraction technique for integral equation methods with higher order basis functions on plane triangles and tetrahedra. *Int. J. Numer. Meth. Eng.* **58**(8), 1149–1165 (2003)
32. Johnson, C.G., Scott, L.R.: An analysis of quadrature errors in second-kind boundary integral methods. *SIAM J. Numer. Anal.* **26**(6), 1356–1382 (1989)
33. Kapur, S., Rokhlin, V.: High-order corrected trapezoidal quadrature rules for singular functions. *SIAM J. Numer. Anal.* **34**, 1331–1356 (1997)
34. Katsurada, M.: A mathematical study of the charge simulation method. II. *J. Fac. Sci. Univ. Tokyo Sect. IA Math.* **36**(1), 135–162 (1989)
35. Khayat, M.A., Wilton, D.R.: Numerical evaluation of singular and near-singular potential integrals. *IEEE Trans. Antennas Propag.* **53**(10), 3180–3190 (2005)
36. Klöckner, A., Barnett, A.H., Greengard, L., O’Neil, M.: Quadrature by expansion: a new method for the evaluation of layer potentials. *J. Comput. Phys.* **252**(1), 332–349 (2013)
37. Kolm, P., Rokhlin, V.: Numerical quadratures for singular and hypersingular integrals. *Comput. Math. Appl.* **41**(3), 327–352 (2001)
38. Kress, R.: Boundary integral equations in time-harmonic acoustic scattering. *Math. Comput. Model.* **15**, 229–243 (1991)
39. Kress, R.: On the numerical solution of a hypersingular integral equation in scattering theory. *J. Comput. Appl. Math.* **61**, 345–360 (1995)
40. Kress, R.: *Linear Integral Equations*. Appl. Math. Sci., vol. 82, second edn. Springer, New York (1999)
41. Lowengrub, J., Shelley, M., Merriman, B.: High-order and efficient methods for the vorticity formulation of the euler equations. *SIAM J. Sci. Comput.* **14**(5), 1107–1142 (1993)
42. Nachtigal, N.M., Reddy, S.C., Trefethen, L.N.: How fast are nonsymmetric matrix iterations? *SIAM J. Matrix Anal. Appl.* **13**(3), 778–795 (1992)
43. Ojala, R., Tornberg, A.K.: An accurate integral equation method for simulating multi-phase Stokes flow. *J. Comput. Phys.* **298**, 145–160 (2015)
44. Olver, F.W.J., Lozier, D.W., Boisvert, R.F., Clark, C.W. (eds.): *NIST Handbook of Mathematical Functions*. Cambridge University Press, Cambridge (2010). <http://dlmf.nist.gov>
45. Pozrikidis, C.: *Boundary Integral and Singularity Methods for Linearized Viscous Flow*. Cambridge Tests in Applied Mathematics. Cambridge University Press, Cambridge (1992)
46. Quaipe, B., Biros, G.: High-volume fraction simulations of two-dimensional vesicle suspensions. *J. Comput. Phys.* **274**, 245–267 (2014)
47. Rachh, M., Klöckner, A., O’Neil, M.: Fast algorithms for quadrature by expansion I: Globally valid expansions. *arXiv preprint* [arXiv:1602.05301](https://arxiv.org/abs/1602.05301) (2016)
48. Rahimian, A., Lashuk, I., Veerapaneni, S.K., Chandramowlishwaran, A., Malhotra, D., Moon, L., Sampath, R., Shringarpure, A., Vetter, J., Vuduc, R., Zorin, D., Biros, G.: Petascale direct numerical simulation of blood flow on 200K cores and heterogeneous architectures. In: 2010 ACM/IEEE International Conference for High Performance Computing, Networking, Storage and Analysis, November, pp. 1–11 (2010)
49. Schwab, C., Wendland, W.L.: On numerical cubatures of singular surface integrals in boundary element methods. *Numer. Math.* **62**(1), 343–369 (1992)
50. Sidi, A., Israeli, M.: Quadrature methods for periodic singular and weakly singular fredholm integral equations. *J. Sci. Comput.* **3**(2), 201–231 (1988)
51. Strain, J.: Locally corrected multidimensional quadrature rules for singular functions. *SIAM J. Sci. Comput.* **16**(4), 992–1017 (1995)
52. Tlupova, S., Beale, J.T.: Nearly singular integrals in 3d Stokes flow. *Commun. Comput. Phys.* **14**(5), 1207–1227 (2013)
53. Tornberg, A.K., Shelley, M.J.: Simulating the dynamics and interactions of flexible fibers in Stokes flows. *J. Comput. Phys.* **196**(1), 8–40 (2004)
54. Trefethen, L.N., Bau III, D.: *Numerical Linear Algebra*. SIAM, Philadelphia (1997)

55. Veerapaneni, S.K., Rahimian, A., Biros, G., Zorin, D.: A fast algorithm for simulating vesicle flows in three dimensions. *J. Comput. Phys.* **230**(14), 5610–5634 (2011)
56. Yarvin, N., Rokhlin, V.: Generalized gaussian quadratures and singular value decompositions of integral operators. *SIAM J. Sci. Comput.* **20**(2), 699–718 (1998)
57. Ying, L., Biros, G., Zorin, D.: A high-order 3D boundary integral equation solver for elliptic PDEs in smooth domains. *J. Comput. Phys.* **216**, 247–275 (2006)
58. Ying, W., Beale, J.T.: A fast accurate boundary integral method for potentials on closely packed cells. *Commun. Comput. Phys.* **14**, 1073–1093 (2013)